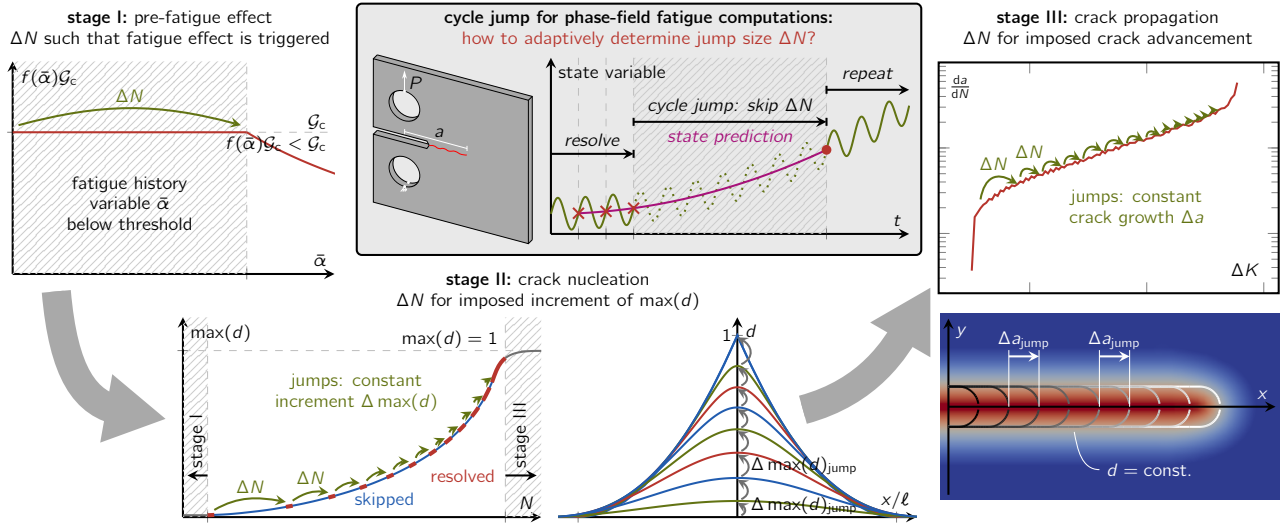


Graphical abstract



An adaptive acceleration scheme for phase-field fatigue computations

Jonas Heinzmann¹, Pietro Carrara¹, Marreddy Ambati², Amir Mohammad Mirzaei³,
Laura De Lorenzis^{1*}

^{1*}Department of Mechanical and Process Engineering, ETH Zürich, Tannenstrasse 3, Zürich, 8092, Switzerland.

²Material Mechanics and Durability, GE Global Research, 1 Research Circle, Niskayuna, 12309, New York, USA.

³Department of Structural, Geotechnical and Building Engineering, Politecnico di Torino, Corso Duca degli Abruzzi 24, Torino, 10129, Italy.

*Corresponding author(s). E-mail(s): ldelorenzis@ethz.ch;

Contributing authors: jheinzmann@ethz.ch; pcarrara@ethz.ch; marreddy.ambati@ge.com;
amir.mirzaei@polito.it;

Abstract

Phase-field models of fatigue are capable of reproducing the main phenomenology of fatigue behavior. However, phase-field computations in the high-cycle fatigue regime are prohibitively expensive due to the need to resolve *spatially* the small length scale inherent to phase-field models and *temporally* the loading history for several millions of cycles. As a remedy, we propose a fully adaptive acceleration scheme based on the cycle jump technique, where the cycle-by-cycle resolution of an appropriately determined number of cycles is skipped while predicting the local system evolution during the jump. The novelty of our approach is a cycle-jump criterion to determine the appropriate cycle-jump size based on a target increment of a global variable which monitors the advancement of fatigue. We propose the definition and meaning of this variable for three general stages of the fatigue life. In comparison to existing acceleration techniques, our approach needs no parameters and bounds for the cycle-jump size, and it works independently of the material, specimen or loading conditions. Since one of the monitoring variables is the fatigue crack length, we introduce an accurate, flexible and efficient method for its computation, which overcomes the issues of conventional crack tip tracking algorithms and enables the consideration of several cracks evolving at the same time. The performance of the proposed acceleration scheme is demonstrated with representative numerical examples, which show a speedup reaching up to four orders of magnitude in the high-cycle fatigue regime with consistently high accuracy.

Keywords: phase-field fatigue, acceleration scheme, cycle jump method, crack tip tracking

1 Introduction

Predictive modeling of fatigue fracture is of interest for a wide range of applications as fatigue is the most common cause of failure for many engineering components [30]. The phase-field modeling approach,

originally proposed for brittle fracture under monotonically increasing loads [9], was recently extended to fatigue (see [2, 11, 60, 59, 4, 24] among many others) and proved able to reproduce the main phenomenological features of fatigue behavior, namely the Wöhler curve, describing the cycle count until failure as a function of the mean load, and the crack growth rate curve, giving the crack propagation rate versus the

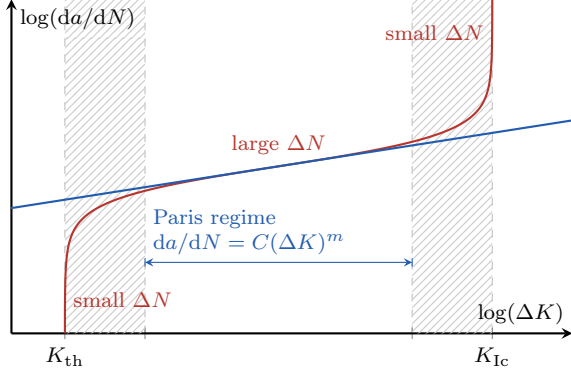


Figure 1: Illustrative crack growth rate curve showing the different regimes of fatigue crack propagation and their relation with a proper cycle jump size ΔN : larger within highly non-linear regimes and smaller during the stable crack propagation or Paris regime.

stress intensity factor amplitude. Phase-field models of fracture are endowed with an internal length scale which is significantly smaller than the characteristic dimensions of the domain under study. In the discretized setting, using e.g. the finite element method, the need to resolve this length leads to fine meshes and thus high computational cost already in quasi-static fracture computations. While various techniques can be used to accelerate the solution of individual time steps, e.g. adaptive mesh refinement (e.g. [25, 29, 19]), special element formulations (e.g. [49, 3]) or solution algorithms (e.g. [21, 35, 13]), an additional issue in fatigue computations is the need to resolve possibly millions of loading cycles. Thus, while computations in the low-cycle fatigue (LCF) regime may still be feasible, computations in the high-cycle fatigue (HCF) and very high-cycle fatigue (VHCF) regimes become impracticable.

Although the slow system evolution within a cycle can be exploited to accelerate the computation of an individual cycle, as done e.g. in [36], the biggest potential for speedup is in the resolution of the cycle domain. Next to multi-time-scale approaches, which aim at separating the processes taking place at different temporal scales (evolution within an individual cycle vs. evolution from cycle to cycle) or temporal homogenization techniques, such as the ones presented in [39, 50, 7], the cycle jump method is a commonly adopted method to speed up fatigue computations due to its straightforward implementation and general applicability. It was first introduced by Lemaitre and Doghri for a damage model with cyclic plasticity in [38], where the core idea is to ‘jump cycles’, i.e. to skip the resolution of blocks of cycles. The evolution of the system during the jumped cycles is predicted by extrapolating selected state variables based on their evolution during a sequence of resolved cycles. The predicted values are

then imposed as a new system state, before the procedure restarts, meaning that again, several cycles are computed to have a basis for the extrapolation of the subsequent cycle jump, and so forth.

In the simplest form of the method, the number of cycles to be jumped, ΔN , is the same for each jump, while no specific criterion is used to decide whether it is appropriate or not to jump at any given point in time. This strategy is applicable only to slowly (almost linearly) evolving systems, and is typically not practicable for fatigue computations. This is illustrated in Fig. 1: during the crack nucleation phase, only a small number of cycles can be jumped due to the strongly non-linear behavior of the system; during stable crack propagation, including the Paris regime, a large number of cycles can be jumped; close to failure, again only a small number of cycles can be jumped. To overcome such limitations, adaptive approaches that tailor the number of cycles to be skipped to the system evolution have been proposed in the literature. The explicit approaches aim at defining ΔN based on the computed states of the system up to the time of the jump, and determine the extension of the jump to keep the error on the system evolution within a given tolerance [14, 47, 52, 15, 34, 46]. This strategy was applied to phase-field fatigue models by Seleš et al in [61] and Haverorth et al in [28], the latter reporting a four-fold reduction of computational time. However, the strategy heavily relies on an allowed error estimate, which the user must set based on geometry, material and loading conditions. Furthermore, these cycle jump approaches typically determine a feasible ΔN at each node or Gauss point, meaning that, out of all locally determined cycle-jump sizes, one suitable for the global system response has to be selected, typically the minimum [61]. Papagem et al. [65] propose to choose the global ΔN based on a percentile of the cumulative distribution of the local cycle-jump sizes. In [68], within an adaptive cycle stepping scheme, a cycle increment is obtained based on a stage-wise defined allowed damage increment, again relying on a crucial user choice for the latter. Another possible strategy involves the adoption of implicit algorithms, where the jump extension is computed accounting also for the state of the system after the jump. For instance, in [42] Loew et al propose to iteratively change the predicted state of the system for a fixed ΔN until the trapezoidal integration rule used for the extrapolation is satisfied within a given tolerance. The arising non-linear equations are solved using a Newton-Raphson scheme involving the computation of a full cycle for each iteration. The authors further propose a method to adaptively determine ΔN , which modulates the cycle-jump size based on the number of iterations that the solver needs to

reach convergence. A similar iterative scheme is combined with adaptive mesh refinement techniques by Jacon et al in [31]. Regardless of being explicit or implicit, the accuracy and speedup of the presented methods critically depend on user-defined parameters, while no method exists to obtain a good estimate for them *a priori*.

To address the issues of existing acceleration schemes, we propose a new adaptive cycle jump (ACJ) algorithm, which is based on the idea of constraining the growth of a representative global variable during the jumped cycles. To this end, the fatigue life of a component is divided into three stages: (I) an initial stage before fatigue effects are triggered, (II) crack nucleation, and (III) crack propagation up to failure. During the first stage, the number of cycles to be skipped is determined so as to jump to the point at which the fatigue effect is triggered for the first time. In the second stage, ΔN is computed such that a target increment of the maximum value of the phase field is obtained, thus progressively approaching the first full crack development. Analogously, in the third stage, ΔN is determined so as to induce a predefined crack length increment. We introduce the concept of a trial cycle after a cycle jump as an *a posteriori* check of the cycle-jump criterion, which allows to automatically correct too optimistic cycle jumps. Further, for the third stage, a novel crack tip tracking algorithm is presented which overcomes the dependency on the spatial discretization and hence the inaccuracy of conventional crack growth monitoring strategies. Using this, the proposed cycle jump scheme can achieve a speedup of up to more than four orders of magnitude while giving consistently low errors with a stable behavior, all without the need to tune any additional parameters. As better clarified later, we introduce optional parameters allowing to prioritize accuracy over speedup or vice versa.

This paper is structured as follows. In Section 2, we briefly overview the phase-field model for brittle fatigue adopted in this paper. Section 3 introduces the ACJ scheme, for which Section 4 presents the concept of the smeared crack length as crack tip tracking algorithm. In Section 5, the behavior and properties of the proposed acceleration scheme are demonstrated, and the obtained accuracy and speedup are compared to those of existing acceleration techniques. Conclusions are drawn in Section 6.

2 Phase-field modeling of brittle fatigue

The phase-field approach to brittle fracture [9] was first derived as the regularization of the formulation in [17], which recasts Griffith's energy criterion [23] into

a variational framework. Later on, it was shown that the same formulation (with a more flexible choice of the involved functions) can be constructed as a special family of gradient damage models [54, 55]. The formulation departs from the total energy functional for a body occupying domain Ω ,

$$\begin{aligned} \mathcal{E}(\mathbf{u}, d) = & \int_{\Omega} [g(d)\psi_+^{\text{el}}(\boldsymbol{\varepsilon}(\mathbf{u})) + \psi_-^{\text{el}}(\boldsymbol{\varepsilon}(\mathbf{u}))] \, dV \\ & + \int_{\Omega} \frac{\mathcal{G}_c}{c_w} \left(\frac{w(d)}{\ell} + \ell |\nabla d|^2 \right) \, dV \\ & - \int_{\partial\Omega_N} \bar{\mathbf{t}} \cdot \mathbf{u} \, dA . \end{aligned} \quad (1)$$

Here, \mathbf{u} is the displacement field, $\boldsymbol{\varepsilon}$ is the infinitesimal strain tensor, $d \in [0,1]$ is the phase-field or damage variable, ℓ is the regularization length, and \mathcal{G}_c is the critical energy release rate. ψ_+^{el} and ψ_-^{el} are respectively the active and the inactive part of the elastic strain energy density, with the active part coupled to the phase field by means of the degradation function $g(d) = (1 - d)^2 + g_0$, where the residual stiffness g_0 is here set to 10^{-6} . Coupling the phase-field only to ψ_+^{el} allows to model contact between crack faces and asymmetric fracture behavior in tension and compression [16, 44, 5, 37, 20, 67]. $w(d)$ is the so-called local dissipation function, for which two common choices are $w(d) = d$ (known as AT1 model) or $w(d) = d^2$ (AT2 model), with the normalization factor c_w equal to 8/3 or 2, respectively. Finally, $\bar{\mathbf{t}}$ is the traction vector acting on the Neumann boundary of the domain, $\partial\Omega_N$. Body forces as well as inertia terms are not considered in this work. Considering an irreversibility constraint for the damage variable (i.e. that the damage can only increase), the unilateral local minimization of the energy (1) with respect to displacement and damage fields in the time-discrete setting delivers the coupled system of governing equations whose solution yields the time-discrete evolution of the two fields. For more details, see [22, 16, 58].

From Griffith's theory, the phase-field approach to brittle fracture inherits the inability to take into account fatigue effects observed under cyclic loading: the crack length a can only grow once the energy release rate \mathcal{G} reaches a critical value \mathcal{G}_c , while fatigue-induced crack nucleation and growth occurs at sub-critical loads. In order to incorporate fatigue effects within a variational framework, a fundamental possibility would be to transition to cohesive zone modeling, as advocated in [43]. Thus far, most of the available investigations depart from the variational framework and develop ad hoc extensions of the classical phase-field

model to account for fatigue phenomena. A popular strategy is to gradually decrease the critical energy release rate \mathcal{G}_c , also known as fracture toughness, as some representative fatigue history variable accumulates, (see [2, 11, 33, 64, 61, 27] and the overview in [1]). An alternative strategy is to introduce an additional dissipative energy contribution accounting for fatigue, which leads the damage driving force to increase as some representative fatigue history variable accumulates, as done e.g. in [8, 4, 10, 28]. Phase-field fatigue models following other strategies exist, e.g. the one presented in [6] which relies on a cyclic plasticity model, or the one presented in [41] which controls fatigue crack growth by a viscous parameter. A comprehensive review of phase-field fatigue models is given in [32].

Another classification criterion for phase-field fatigue models is the temporal domain in which the model is formulated: for the formulation in the physical (pseudo-) time domain t , the loading history is to be resolved with several steps per cycle following the path of repetitive loading and unloading. Alternatively, the model can also be formulated directly in the cycle domain where a surrogate loading sequence replaces the individual steps within a cycle, allowing for an efficient computation of several representative cycles at once, such as e.g. in [60, 24, 36]. This does not alleviate the inherent history-dependency introduced with the fatigue effects, accompanied by the non-linearity in the cycle domain, implying that for both modeling strategies the computational cost is high.

To develop and benchmark our acceleration scheme for phase-field fatigue computations, we adopt the model in [11] (extending the one-dimensional model in [2]), which served as the basis for many modifications and extensions, e.g. [33, 64, 63, 61, 62, 27]. The core idea is to introduce a *fatigue history variable* $\bar{\alpha}$ to capture the locally endured fatigue effect. In the mean-load independent version of the model, the fatigue history variable is defined as [11]

$$\bar{\alpha}(\mathbf{x}; t) = \int_0^t H(\alpha \dot{\alpha}) |\dot{\alpha}| d\tau, \quad (2)$$

that is the temporal accumulation of a local variable $\alpha(\mathbf{x})$ representing the ‘local fatigue effect’. The Heaviside function H ensures that the fatigue effects are only accumulated during loading phases. The variable α is defined as the degraded active part of the elastic energy density $g(d)\psi_+^{\text{el}}$. With this definition, the fatigue effect evolves faster around the crack tip. The fatigue history variable enters the so-called *fatigue degradation function* $f(\bar{\alpha}) \in [0, 1]$ to modulate the fracture toughness

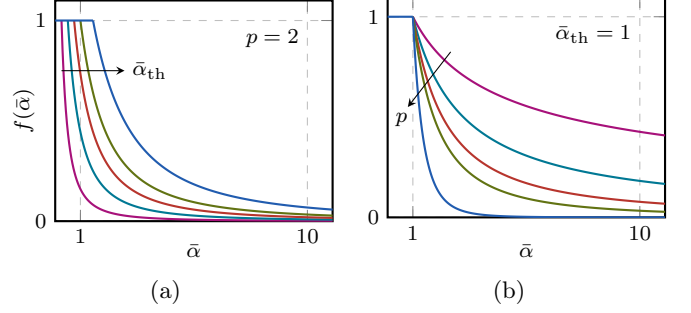


Figure 2: Fatigue degradation function $f(\bar{\alpha})$ with the influence of its parameters $\bar{\alpha}_{\text{th}}$ (a) and p (b).

of the material \mathcal{G}_c . It is defined as

$$f(\bar{\alpha}) = \begin{cases} 1 & \bar{\alpha} < \bar{\alpha}_{\text{th}} \\ \left(1 - \frac{\bar{\alpha} - \bar{\alpha}_{\text{th}}}{\bar{\alpha} + \bar{\alpha}_{\text{th}}}\right)^p & \bar{\alpha} \geq \bar{\alpha}_{\text{th}} \end{cases}. \quad (3)$$

This is slightly different from the one proposed in [11], and features two parameters p and $\bar{\alpha}_{\text{th}}$ that can be calibrated using a limited set of experimental data (e.g., Wöhler and crack growth rate curves) and that allow more flexibility in reproducing different behaviors. The latter acts as a threshold for $\bar{\alpha}$, governing the point at which the fatigue effect is triggered for the first time, while p influences the rate of degradation, as illustrated in Fig. 2.

With these definitions, the rate of the total energy functional for the brittle fatigue fracture model reads

$$\begin{aligned} \dot{\mathcal{E}}(\mathbf{u}, d; \bar{\alpha}) = & \int_{\Omega} g(d) \frac{\partial \psi_+^{\text{el}}}{\partial \boldsymbol{\varepsilon}} : \dot{\boldsymbol{\varepsilon}} + \frac{\partial \psi_-^{\text{el}}}{\partial \boldsymbol{\varepsilon}} : \dot{\boldsymbol{\varepsilon}} + g'(d) \psi_+^{\text{el}} \dot{d} dV \\ & + \int_{\Omega} f(\bar{\alpha}) \frac{\mathcal{G}_c}{c_w} \left(\frac{w'(d)}{\ell} \dot{d} + 2\ell \nabla d \cdot \nabla \dot{d} \right) dV \\ & - \int_{\partial\Omega_N} \bar{\mathbf{t}} \cdot \dot{\mathbf{u}} dA. \end{aligned} \quad (4)$$

Departing from a fully variational formulation, $\bar{\alpha}$ is treated as a parameter of the energy functional to derive the governing equations of the coupled field problem. The balance of linear momentum and the Neumann and Dirichlet boundary conditions read

$$\begin{aligned} \nabla \cdot \boldsymbol{\sigma} &= \mathbf{0} & \forall \mathbf{x} \in \Omega \\ \boldsymbol{\sigma} \cdot \mathbf{n} &= \bar{\mathbf{t}} & \forall \mathbf{x} \in \partial\Omega_N \\ \mathbf{u} &= \bar{\mathbf{u}} & \forall \mathbf{x} \in \partial\Omega_D \end{aligned} \quad (5)$$

with the Cauchy stress definition $\boldsymbol{\sigma} := g(d) \partial \psi_+^{\text{el}} / \partial \boldsymbol{\varepsilon} + \partial \psi_-^{\text{el}} / \partial \boldsymbol{\varepsilon}$. Here \mathbf{n} is the outward normal unit vector to the boundary and $\partial\Omega_D$ is the Dirichlet boundary

on which $\bar{\mathbf{u}}$ is the prescribed displacement. The evolution equations and boundary conditions for the damage variable, due to the postulated irreversibility of damage, are expressed as Karush-Kuhn-Tucker conditions as follows

$$\begin{cases} \dot{d} \geq 0 \\ 2(1-d)\psi_+^{\text{el}} - \frac{f(\bar{\alpha})\mathcal{G}_c}{c_w} \left(\frac{w'(d)}{\ell} - 2\ell \nabla \cdot (\nabla d) \right) \\ \quad + \frac{2\mathcal{G}_c\ell}{c_w} \nabla f(\bar{\alpha}) \cdot \nabla d \leq 0 \\ \left[2(1-d)\psi_+^{\text{el}} - \frac{f(\bar{\alpha})\mathcal{G}_c}{c_w} \left(\frac{w'(d)}{\ell} - 2\ell \nabla \cdot (\nabla d) \right) \right. \\ \quad \left. + \frac{2\mathcal{G}_c\ell}{c_w} \nabla f(\bar{\alpha}) \cdot (\nabla d) \right] \dot{d} = 0 \end{cases} \quad \forall \mathbf{x} \in \Omega \quad (6a)$$

$$\begin{cases} \dot{d} \geq 0 \\ \nabla d \cdot \mathbf{n} \geq 0 \\ (\nabla d \cdot \mathbf{n}) \dot{d} = 0 \end{cases} \quad \forall \mathbf{x} \in \partial\Omega. \quad (6b)$$

Evolution of the phase-field is only possible once the crack driving force has reached a critical level, which however now depends on the loading history by means of $f(\bar{\alpha})$.

3 Adaptive acceleration scheme based on a cycle-jump criterion

This section addresses the issue of the high cost associated with phase-field fatigue computations by proposing a novel acceleration scheme.

3.1 Outline of the scheme

We adopt the cycle jump technique due to its straightforward implementation, minimal additional computational cost and general applicability to any type of model formulation. As schematically illustrated in Fig. 3, the strategy is to resolve some cycles (i.e. compute an appropriate number of load steps during these cycles, as explained later, these are also denoted as high-fidelity or HF computations), extrapolate the further evolution of the system, then jump ΔN cycles, then again resolve some cycles, and so forth. Thus, the two core ingredients of the scheme are

- (i) the choice of a *local* state variable to be extrapolated to predict the state after the jumped cycles, as well as a strategy to extrapolate it, and
- (ii) the choice of a *global* state variable and of a criterion based on which to decide whether and, if so, how many cycles can be jumped.

3.2 Extrapolation of the local system state

As for the first ingredient, we select the fatigue history variable $\bar{\alpha}$. The starting point for the extrapolation of $\bar{\alpha}$ in the cycle domain is a Taylor series expansion at the last resolved cycle preceding a cycle jump up to the quadratic term to account for non-linear system evolution. It reads

$$\begin{aligned} \bar{\alpha}(\mathbf{x}, N + \Delta N) &= \bar{\alpha}(\mathbf{x}, N) + \dot{\bar{\alpha}}(\mathbf{x}, N) \Delta N \\ &\quad + \ddot{\bar{\alpha}}(\mathbf{x}, N) \frac{\Delta N^2}{2} + \mathcal{O}(\Delta N^3), \end{aligned} \quad (7)$$

where $\dot{\bar{\alpha}} = \partial \bar{\alpha} / \partial N$ and $\ddot{\bar{\alpha}} := \partial^2 \bar{\alpha} / \partial N^2$. These cycle-wise derivatives are approximated using backwards finite differences (FDs), and we consider a stencil of $N_s = 4$ cycles to be computed between cycle jumps, resulting in

$$\begin{aligned} \bar{\alpha}(\mathbf{x}, N + \Delta N) &\approx \bar{\alpha}^*(\mathbf{x}, N + \Delta N) = \bar{\alpha}(\mathbf{x}, N) \\ &\quad + \frac{1}{6} [-2\bar{\alpha}(\mathbf{x}, N-3) + 9\bar{\alpha}(\mathbf{x}, N-2) \\ &\quad \quad - 18\bar{\alpha}(\mathbf{x}, N-1) + 11\bar{\alpha}(\mathbf{x}, N)] \Delta N \\ &\quad + \frac{1}{2} [-\bar{\alpha}(\mathbf{x}, N-3) + 4\bar{\alpha}(\mathbf{x}, N-2) \\ &\quad \quad - 5\bar{\alpha}(\mathbf{x}, N-1) + 2\bar{\alpha}(\mathbf{x}, N)] \Delta N^2. \end{aligned} \quad (8)$$

Since the state variable to be predicted is a local quantity, the extrapolation must be performed for each point \mathbf{x} . However, the FD-based scheme has a limited computational cost.

3.3 Cycle-jump criterion

In the following, we expand on the second ingredient, i.e. the cycle-jump criterion based on the value of a global variable.

3.3.1 Need for a cycle-jump criterion

We schematically motivate the adaptive determination of ΔN in Fig. 4. For simplicity, we assume a single fatigue crack propagating stably along the \tilde{x} direction and illustrate the qualitative trend of the fatigue history variable $\bar{\alpha}$ along \tilde{x} as a function of the cycle count. $\bar{\alpha}$ is maximum at the crack tip and gradually decreases away from it, and the location of the crack tip changes from cycle to cycle. If the crack tip position after a cycle jump is sufficiently close to the one prior to it, the local extrapolation of $\bar{\alpha}$ yields acceptable prediction errors, such as for the smaller cycle jump in Fig. 4. In contrast, if the crack tip position after a jump is far from the one before the jump, the extrapolation is not accurate, resulting in a large prediction error,

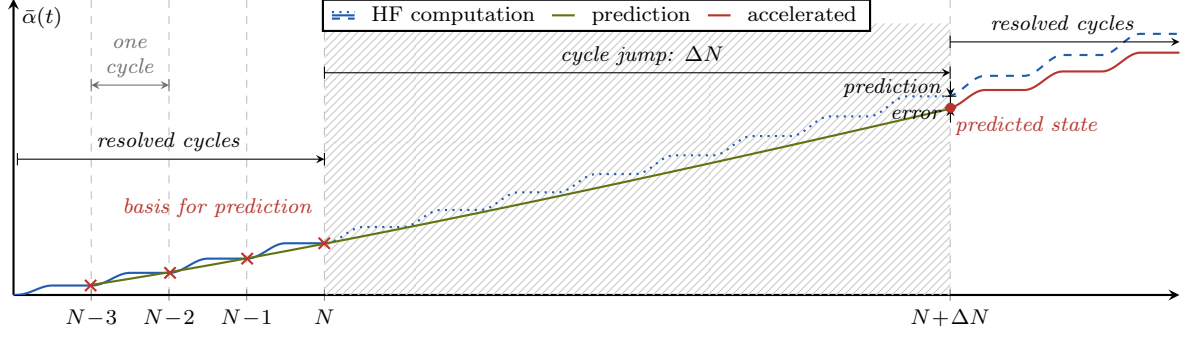


Figure 3: Illustrative representation of the cycle jump technique in terms of the evolution of the fatigue history variable $\bar{\alpha}$ and comparison with the HF computations. Several cycles are computed and used as basis for the extrapolation of the system evolution over ΔN cycles. Then, the prediction is enforced and the procedure can start over.

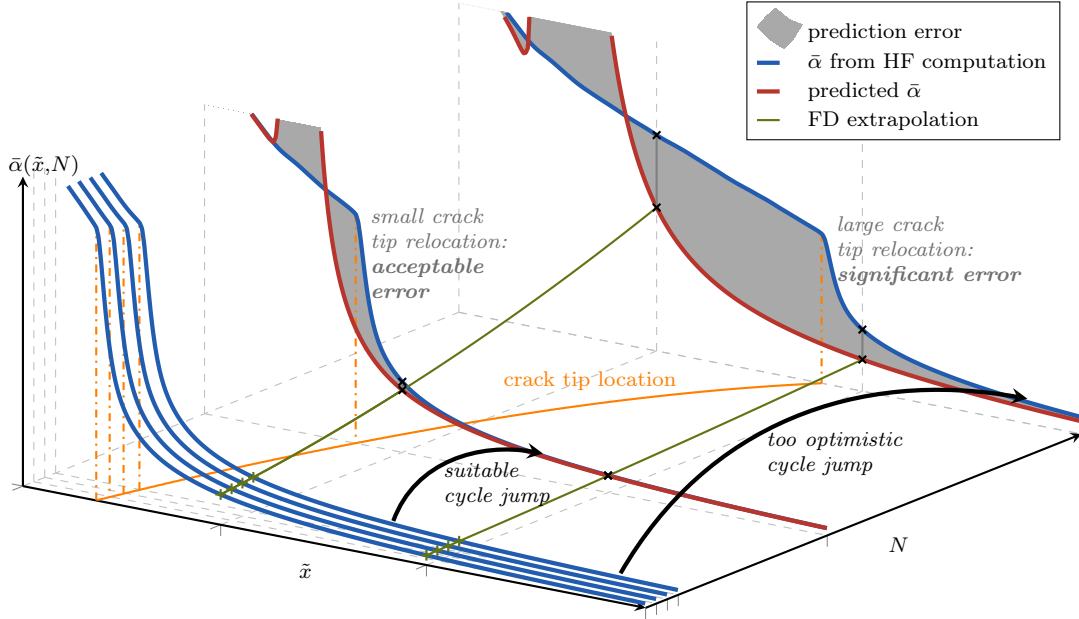


Figure 4: Accuracy of the FD-based extrapolation (8) in comparison to HF computations for two different cycle jump extensions. The blue lines depict the profile of the fatigue history variable $\bar{\alpha}$ ahead of the crack tip along the crack path coordinate \tilde{x} . A suitable cycle jump with a small crack tip relocation yields a smaller prediction error (gray surfaces) compared to an overly optimistic jump with a large crack tip relocation during the skipped cycles.

such as for the larger cycle jump in Fig. 4. Hence, the cycle-jump size ΔN during crack propagation must be chosen such that the relocation of the crack tip lies within certain bounds.

The generalization of this concept to all stages of the fatigue life is the simple idea behind the proposed ACJ: determine ΔN such that, during the jumped cycles, the state of the system is only advancing to a predefined extent. In the following, we formalize the above idea.

3.3.2 Computation of the number of jumped cycles

We define a *global* variable $\Lambda(N)$ which is representative of the current system state from the standpoint

of fatigue; the selection of an appropriate variable is discussed in the next subsection. We then introduce a cycle-jump criterion

$$\underbrace{\Lambda(\bar{N})}_{\text{post-jump}} \stackrel{!}{=} \underbrace{\Lambda(N)}_{\text{pre-jump}} + \underbrace{\Delta\bar{\Lambda}}_{\text{target increment}} \quad (9)$$

imposing a target increment $\Delta\bar{\Lambda}$ of Λ during a cycle jump. Thus, we aim at computing the cycle count $\bar{N} := N + \Delta N$ at which the representative variable takes the value $\Lambda(N) + \Delta\bar{\Lambda}$. By approximating the left-hand side with a quadratic function

$$\Lambda(\bar{N}) \approx \Lambda^*(\bar{N}) = \tilde{\Lambda}_2 \bar{N}^2 + \tilde{\Lambda}_1 \bar{N} + \tilde{\Lambda}_0, \quad (10)$$

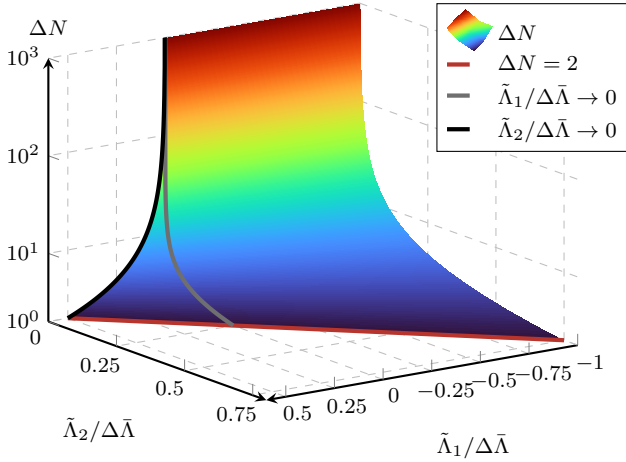


Figure 5: Obtained cycle-jump size ΔN for a range of the normalized fitting parameters $\tilde{\Lambda}_1/\Delta\bar{\Lambda}$ and $\tilde{\Lambda}_2/\Delta\bar{\Lambda}$. The red line limits the parameter range where the minimum cycle jump size $\Delta N = 2$ is obtained, and the black and gray lines represent a purely linear and a purely quadratic fit, respectively.

where $\tilde{\Lambda}_0$, $\tilde{\Lambda}_1$ and $\tilde{\Lambda}_2$ are fitting parameters, the cycle-jump criterion can be rewritten as

$$\tilde{\Lambda}_2 \bar{N}^2 + \tilde{\Lambda}_1 \bar{N} + \tilde{\Lambda}_0 - \Lambda(N) - \Delta\bar{\Lambda} = 0. \quad (11)$$

Based on (11), an explicit expression can be found for \bar{N} and hence for ΔN ,

$$\Delta N = \text{round} \left(\frac{-\tilde{\Lambda}_1 + \sqrt{\tilde{\Lambda}_1^2 - 4\tilde{\Lambda}_2(\tilde{\Lambda}_0 - \Lambda(N) - \Delta\bar{\Lambda})}}{2\tilde{\Lambda}_2} \right) - N, \quad (12)$$

where we have assumed that Λ^* is monotonically increasing for $\bar{N} > 0$. This is ensured by choosing Λ such that it only grows during the fatigue life, as we explain later. Further, since the cycle count is an integer, the determined value must be rounded to the nearest natural number. The obtained cycle-jump size as a function of the normalized fitting parameters $\tilde{\Lambda}_1/\Delta\bar{\Lambda}$ and $\tilde{\Lambda}_2/\Delta\bar{\Lambda}$ is visualized in Fig. 5. Note that for illustrative purposes and without loss of generality, in Fig. 5, $\tilde{\Lambda}_0 = \Lambda(N)$ is assumed (meaning that the quadratic approximation matches the intercept of Λ) and the term $-N$ in (12) is neglected. We can observe that the cycle-jump size rapidly grows as the fitting parameters tend towards zero, since the slower the evolution of Λ , the more cycles are necessary to obtain the target increment $\Delta\bar{\Lambda}$. This manifests the adaptivity of the acceleration scheme.

To obtain the fitting parameters of the quadratic function $\tilde{\Lambda}_{0,1,2}$, we use a linear least squares (LLSQ) fit. To ensure sufficient robustness in the computation of ΔN , the quadratic function is fitted onto data points of Λ during the last $3N_s$ computed cycles, i.e. ranging

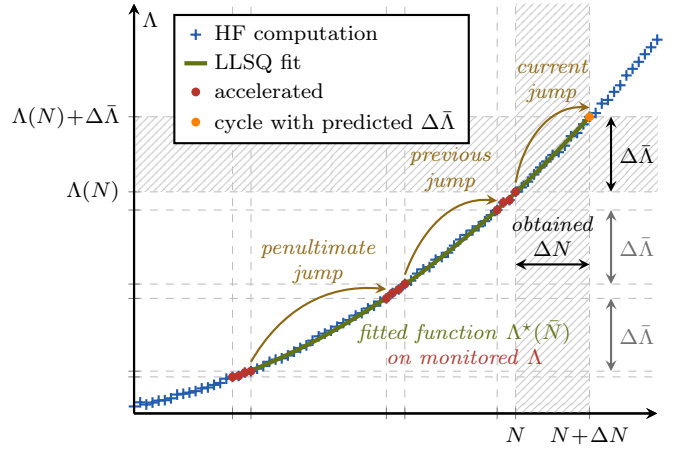


Figure 6: LLSQ fit of the evolution of the representative global state variable Λ and cycle jump size ΔN determined based on the target increment $\Delta\bar{\Lambda}$.

up to the penultimate cycle jump. This is especially crucial for the stability of the acceleration scheme in the HCF regime, where Λ may evolve very slowly. Since only a short segment of the evolution of Λ is represented by the quadratic interpolation (10), the fitting parameters $\tilde{\Lambda}_{0,1,2}$ must be re-determined prior to any individual cycle jump. The LLSQ fit on the data points between three consecutive cycle jumps and the general concept of the outlined approach are illustrated in Fig. 6, where the various cycle jumps lead to the same $\Delta\bar{\Lambda}$, although achieved with different cycle-jump sizes.

3.3.3 Automatic transition to high-fidelity computation

It is worth noting that the fatigue computations are only accelerated if (12) delivers $\Delta N \geq 2$, which by virtue of (11) can be translated into feasible ranges of the fitting parameters $\tilde{\Lambda}_1$ and $\tilde{\Lambda}_2$, namely

$$4\tilde{\Lambda}_2 + 2\tilde{\Lambda}_1 \leq \Delta\bar{\Lambda}, \quad (13)$$

again assuming $\tilde{\Lambda}_0 = \Lambda(N)$ and neglecting the term $-N$ in (12) for illustrative purposes without loss of generality. This is drawn as the red limit curve in Fig. 5. The minimum number of cycles to be jumped corresponds to the rate of system evolution being so large that the acceleration scheme naturally reverts to a HF analysis. I.e., once the algorithm determines that the evolution of the system is too fast by obtaining $\Delta N < 2$, no jump is performed. At very low load levels, this transition to the full resolution of the remaining fatigue life may occur very late within the fatigue life or not at all; for higher load levels, it may happen relatively early, far from failure. Further, at load levels close to monotonic failure, the algorithm does not skip cycles since the system evolution is too fast.

3.3.4 Special cases

Despite the choice of a monotonically increasing Λ , in a numerical context with the fitted function Λ^* , two special cases must be addressed. The first special case occurs if (12) does not have a real solution, i.e. the parabola described by the quadratic ansatz (12) does not obtain the target value of $\Lambda(N) + \Delta\bar{\Lambda}$ for any real ΔN . In this case, we revert to a linear approximation of the evolution of Λ , i.e. we neglect the quadratic term and compute a cycle-jump size of

$$\Delta N = \text{round} \left(\frac{\Lambda(N) + \Delta\bar{\Lambda} - \tilde{\Lambda}_{0,\text{lin}}}{\tilde{\Lambda}_{1,\text{lin}}} \right) - N \quad (14)$$

if $\tilde{\Lambda}_1^2 - 4\tilde{\Lambda}_2(\tilde{\Lambda}_0 - \Lambda(N) - \Delta\bar{\Lambda}) < 0$.

Clearly, the fitting parameters $\tilde{\Lambda}_{p,\text{lin}}$ need to be re-determined. The second special case occurs if (12) yields a negative cycle-jump size. This may occur in the VHCF regime with extremely slow system evolution. In this case, we simply use half of ΔN of the last successfully performed cycle jump.

3.4 Choice of the global monitoring variable and of its target increment

For the proposed strategy, the choice of Λ and $\Delta\bar{\Lambda}$ plays a central role. Further, Λ must be monotonically increasing as the fatigue effects advance. Due to the diversity of the system behavior in different phases of its fatigue life, no single choice for Λ is appropriate for all phases. Thus, we select a different Λ in each of three fatigue life stages, as depicted in Fig. 7 and described in the following.

3.4.1 Stage I: pre-fatigue effect

As outlined in Section 2, the adopted phase-field fatigue model features a threshold value $\bar{\alpha}_{\text{th}}$ of the fatigue history variable, prior to which no fatigue effects take place. Thus, this initial stage clearly satisfies

$$\max_{\mathbf{x}} (\bar{\alpha}(\mathbf{x})) \leq \bar{\alpha}_{\text{th}} . \quad (15)$$

As depicted in Fig. 8a, the fatigue history variable $\bar{\alpha}$ accumulates linearly from cycle to cycle during stage I, since $\bar{\alpha} < \bar{\alpha}_{\text{th}}$. Consequently, the system behaves linear-elastically and it is possible to jump directly to the point where the fatigue effect is triggered for the first time, which can be determined analytically due to the linear growth. This means that for the first stage, the choice for Λ is $\max(\bar{\alpha}(\mathbf{x}))$ while the target

increment $\Delta\bar{\Lambda}$ is

$$\Delta \max(\bar{\alpha}(\mathbf{x})) = \bar{\alpha}_{\text{th}} - \max(\bar{\alpha}(\mathbf{x})) . \quad (16)$$

Essentially, this makes for an initial cycle jump similar to the one presented in [61] where the cycle regime without fatigue effects is skipped directly. As indicated in Fig. 8a, the first N_s cycles must be resolved to obtain a basis for the LLSQ fit. The achievable speed up in stage I depends on the chosen fatigue history variable threshold $\bar{\alpha}_{\text{th}}$ as well as the loading; in general however, stage I amounts to a rather small portion of the overall fatigue lifetime.

3.4.2 Stage II: fatigue crack nucleation

Once the fatigue threshold is met, fatigue effects start. The damage variable, initially zero, evolves until at some location the first fully developed damage localization profile (the smeared representation of a crack) appears, i.e. at some point it is $d > 1 - \text{TOL}$, where we choose $\text{TOL} = 0.01$. Thus, Λ is $\max(d(\mathbf{x}))$, and the second stage is identified by

$$\max_{\mathbf{x}} (d(\mathbf{x})) \leq 0.99 . \quad (17)$$

The stage-II cycle jump splits this range by imposing equal increments of $\Delta \max(d)$, as illustrated in Fig. 9. The largest cycle jumps are obtained in the beginning of the stage with relatively slow system evolution, while towards the end of the stage, ΔN becomes smaller. If $\max(d)$ evolves too quickly, as illustrated in Fig. 9, the determined cycle-jump size is $\Delta N < 2$, hence no further cycles are skipped and the remaining cycles are resolved. We propose a target increment $\Delta\bar{\Lambda}$ of 0.02 in this second stage. To provide flexibility, a scalar factor $\lambda_{\text{II}} > 0$ is introduced to influence this baseline, i.e.

$$\Delta \max(d(\mathbf{x})) = \lambda_{\text{II}} 0.02 . \quad (18)$$

This means that for $\lambda_{\text{II}} > 1$, the target increment during the cycle jump is larger than the baseline, obtaining larger ΔN which increase the speedup but decrease the accuracy of the fatigue computations. Conversely, for $\lambda_{\text{II}} < 1$, the accuracy improves with smaller cycle jumps, while the speedup decreases. With the default choice of $\lambda_{\text{II}} = 1$, the acceleration scheme in our numerical experiments always yields a good compromise between speedup and accuracy, independently of the specimen, material or load level, as shown in Section 5.

3.4.3 Stage III: fatigue crack propagation

After the formation of the first crack, the crack grows, first stably, and finally unstably, until failure at N_u . In

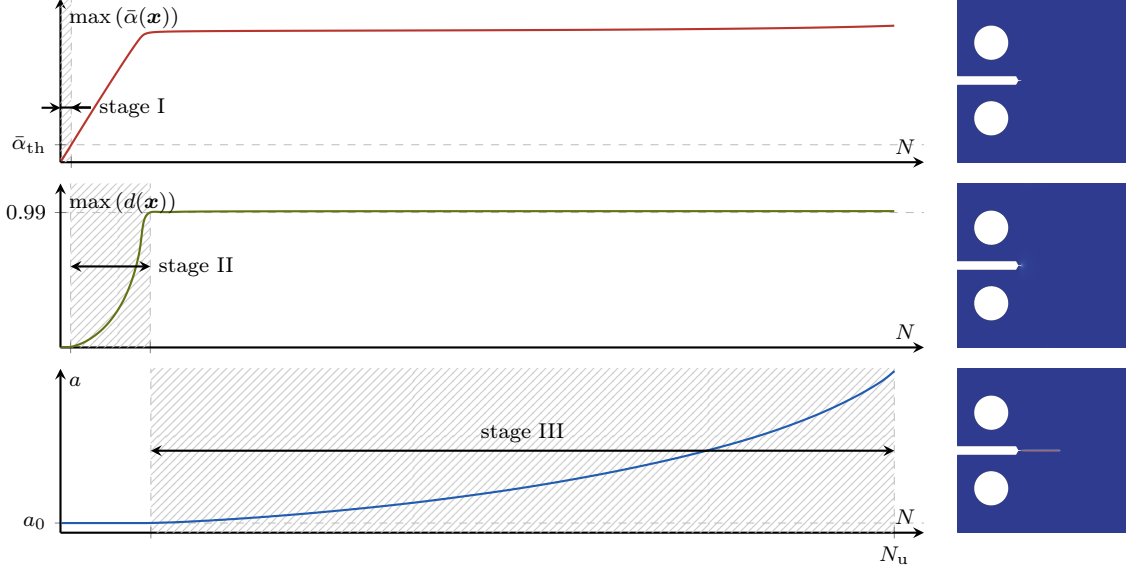


Figure 7: Stages I, II and III of the fatigue lifetime for a phase-field fatigue model in terms of the monitored global state quantities $\max(\bar{\alpha})$, $\max(d)$ and crack length a . On the right-hand side, exemplary phase-field states from a representative test are depicted.

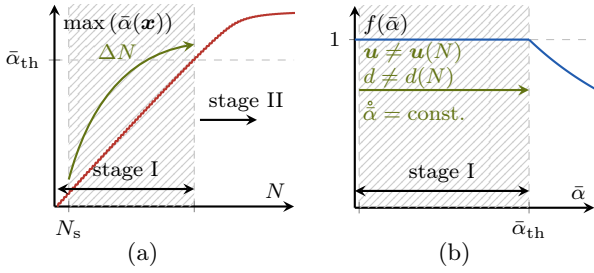


Figure 8: Evolution of $\max(\bar{\alpha})$ in the first stage (a) and behavior of the fatigue degradation function $f(\bar{\alpha})$ (b).

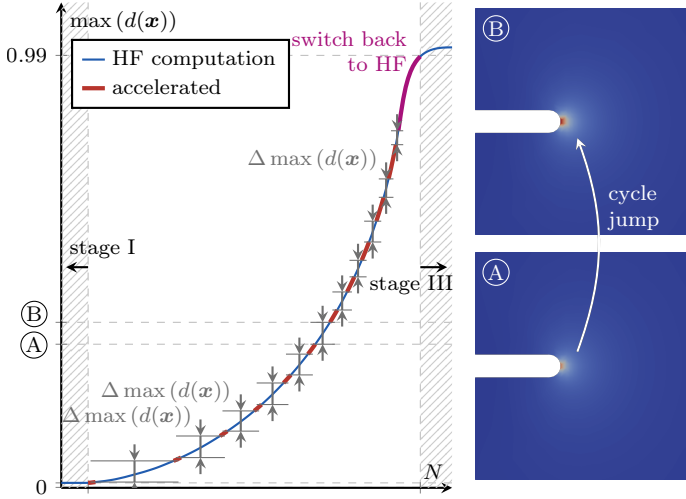


Figure 9: Comparison between the HF and the ACJ evolution of $\max(d)$ in the second stage of the fatigue life (left) and evolution of the phase-field variable at two representative points A and B. The ACJ criterion is defined so as to trigger a constant increment of $\Delta \max(d)$ during a cycle jump.

this stage, the crack length itself, a , is the most representative monitoring quantity for Λ which satisfies

$$a \leq a_u, \quad (19)$$

with a_u as the crack length at failure. To fix ideas, we consider here a single fatigue crack, while the approach is able to account for multiple fatigue cracks propagating at the same time, see Section 4. As will be shown with the numerical examples in Section 5, most cycle jumps occur in this stage during stable crack propagation. In stage III, the target increment Δa must be associated to the size of the zone with dominant fatigue effect. This is why we define the feasible increment $\Delta \bar{\Lambda}$ in stage III as

$$\Delta a = \lambda_{\text{III}} \frac{\ell}{2}. \quad (20)$$

Analogously to stage II, a parameter $\lambda_{\text{III}} > 0$ is introduced for more flexibility. Again, $\lambda_{\text{III}} > 1$ allows for larger crack propagation during a cycle jump resulting in higher speedup and lower accuracy, and vice versa for $\lambda_{\text{III}} < 1$. The cycle jumps of stage III can be interpreted as a subdivision of the total crack length into multiple jumps with uniform crack increments, as portrayed in Fig. 10. Due to the ever increasing crack growth rate \dot{a} for a standard fatigue test setup (Fig. 1), also in stage III the cycle-jump size decreases during the progression of the fatigue life.

The choice of the crack length a as representative variable within stage III raises the challenge of how to precisely monitor the crack length in a numerical context. Conventional crack tip tracking algorithms monitor no crack growth below the discretization length,

which would cause the proposed scheme to fail in the HCF regime. To overcome this and further issues, we introduce the notion of the ‘smeared crack length’ in Section 4.

An overview of the resulting stage-wise acceleration scheme is given in Tab. 1 in terms of stage definition, representative variable Λ as well as target increment $\Delta\bar{\Lambda}$ thereof during a jump. For an external loading which causes $\max(\bar{\alpha}(\mathbf{x})) > \bar{\alpha}_{\text{th}}$ already in the first cycle, the computation directly starts in stage II; if the external loading leads to full crack development already in the first cycle, only stage III remains.

3.4.4 Estimate of the number of cycles to be resolved

A noteworthy feature of the proposed approach is that, given the domain geometry and material parameters, nearly the same total number of cycles must be computed for the total fatigue life regardless of the specific rate of system evolution, which we illustrate in the following. Since the cycle-jump criterion ensures the target increment $\Delta\bar{\Lambda}$ of the global monitoring variable, the number of cycles to be resolved N_r can be estimated as follows

$$N_{r,\text{est}} = \underbrace{N_s}_{\text{stage I}} + \underbrace{\frac{0.99}{\lambda_{\text{II}}0.02}N_s}_{\text{stage II}} + \underbrace{\frac{a_u}{\lambda_{\text{III}}\ell/2}N_s}_{\text{stage III}}. \quad (21)$$

While for the first stage a single cycle jump is necessary, for the other stages the number of cycle jumps originates from the total range of the representative variable divided by the imposed increment. N_s cycles have to be computed in between the individual cycle jumps, and hence N_s cycles are counted per cycle jump within each stage. Thus, the number of cycles to be resolved only depends on the speedup parameters, N_s and a_u/ℓ . As an example, with speedup parameters $\lambda_{\text{II}} = \lambda_{\text{III}} = 1$, $N_s = 4$ and assuming $a_u = 100\ell$, this results in 1002 cycles which need to be resolved. Note that this estimate assumes that the system predominantly evolves during the cycle jumps and exhibits a negligible system evolution within resolved cycles, which is the case for HCF computations; for LCF computations, the system shows a substantial evolution also during the cycles between cycle jumps, meaning that less cycles than estimated need to be resolved. The validity of this estimate is shown later with numerical examples. Note that for $\lambda_{\text{II,III}} > 1$, the total number of cycles to be resolved decreases, while for $\lambda_{\text{II,III}} < 1$ the number of resolved cycles increases. Also, the speedup parameters λ_{II} and λ_{III} allow to influence the accuracy of the stage of crack nucleation or crack propagation independently. An inverse consideration to (21) can

be made, meaning that the speedup parameters can be tuned based on the number of computationally affordable cycles.

3.5 Algorithmic aspects

To conclude this section, we address algorithmic aspects relevant for the implementation of the scheme. A flowchart is shown in Fig. 11. The procedure starts by resolving a cycle, i.e. solving multiple load steps with an iterative solution procedure, as detailed in Fig. 11b. After each resolved cycle, the monitoring variables are computed. Furthermore, the $\bar{\alpha}$ field is saved for the last N_s computed cycles.

After the end of a cycle, the algorithm checks based on the cycle count whether a cycle jump can be performed: since the last executed cycle jump to the current cycle number N_{last} , at least N_s cycles must have been computed to have a basis for the FD-based system state prediction. If this is not the case, the next cycle is resolved again, otherwise, the algorithm determines in which stage of fatigue life the system is based on the value of the variables $\max(\bar{\alpha}(\mathbf{x}))$ and $\max(d(\mathbf{x}))$. Then, the extension of the cycle-jump ΔN is computed using (12) and considering the special cases in Section 3.3.4. For this, the LLSQ fit is performed on the data points of Λ from the last $3N_s$ computed cycles (at the beginning of the computations where less data points are available, all available data points are used, i.e. $1N_s$ or $2N_s$ for the first and second cycle jump, respectively). If a cycle-jump size $\Delta N < 2$ is obtained, no cycle jump is performed, but the next cycle is again resolved. In the case of $\Delta N \geq 2$, the system state at $N + \Delta N$ is predicted with the FD-based extrapolation (8). To enforce the irreversibility of the fatigue process $\dot{\bar{\alpha}} \geq 0$, any negative increments are neglected in the FD-based extrapolation of $\bar{\alpha}$ (such values may occur when the system evolution rate is close to numerical tolerances in the VHCF regime).

After the cycle jump, we compute the cycle number $N + \Delta N$, i.e. the cycle for which the monitoring variable is expected to be $\Lambda(N) + \Delta\bar{\Lambda}$, which we denote as *trial cycle* since it is the cycle at which we decide whether to accept or reject the cycle jump. This cycle follows exactly the same procedure as a regular resolved cycle illustrated in Fig. 11b, with the difference that $\bar{\alpha}$ is not updated during the solution procedure, since its value at the end of the trial cycle is already known. The trial cycle serves several purposes:

- By computing the system state at $N + \Delta N$, the equilibrium of the system is re-established with the extrapolated state variable.
- Instead of computing only the last load step of the cycle $N + \Delta N$, the whole trial cycle is resolved before accepting the cycle jump. If any of the tested

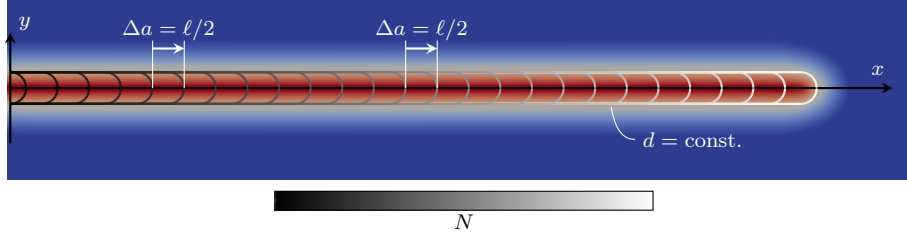


Figure 10: Discretization of the phase-field crack by means of cycle jumps with a constant crack increment Δa in stage III. The contour lines of the phase field indicate different crack lengths in between the cycle jumps.

Table 1: Stage-wise characteristics of the ACJ scheme.

stage	stage identification	Λ	$\Delta\bar{\Lambda}$	comments
I	$\max(\bar{\alpha}(\mathbf{x})) \leq \bar{\alpha}_{\text{th}}$	$\max(\bar{\alpha}(\mathbf{x}))$	$\bar{\alpha}_{\text{th}} - \max(\bar{\alpha}(\mathbf{x}))$	linear evolution after first full cycle for chosen model [11]
II	$\max(d(\mathbf{x})) \leq 0.99$	$\max(d(\mathbf{x}))$	$\lambda_{\text{II}} 0.02$	
III	$\max(d(\mathbf{x})) > 0.99$	a	$\lambda_{\text{III}} \ell/2$	smeared crack length for crack tip tracking (Section 4.2)

load steps of the trial cycle do not converge, implying that the system equilibrium could not be established with the extrapolated state variables (e.g. due to a too optimistic cycle jump), the state prior to the jump is restored. Then, another cycle jump is tried with half of the last accepted cycle-jump size. Only if all load steps of the trial cycle converge, the cycle jump is accepted.

- Finally, the trial cycle allows to determine the satisfaction of the cycle-jump criterion (9) during the skipped cycles, i.e. an *a posteriori* error evaluation. For this, the growth $\Delta\Lambda_{\text{tr}}$ determined after the trial cycle is compared to the target increment $\Delta\bar{\Lambda}$. If the cycle-jump criterion is violated by more than 50%, the old state is restored and the jump size for the next trial is adjusted to

$$\Delta N_{\text{new}} = \text{round} \left(\frac{\Delta\bar{\Lambda}}{\Delta\Lambda_{\text{tr}}} \Delta N \right) \quad \text{if } \Delta\Lambda_{\text{tr}} > 1.5\Delta\bar{\Lambda} . \quad (22)$$

The computational effort for the trial cycle is not wasted, since the system state at $N + \Delta N$ can be used as basis for the following cycle jump, hence only $N_s - 1$ cycles remain to be computed prior to the next cycle jump. Note that the adjustment of the cycle-jump size after non-convergence, or non-satisfaction of the cycle-jump criterion is only rarely necessary in the VHCF regime or close to transitions between stages, as demonstrated later with numerical examples.

3.6 Applicability of the approach

Although the approach was presented with the model presented in [11], it is applicable to any other phase-field fatigue model. This is due to the general definition of the three stages of the fatigue lifetime as well as the universal definition of the cycle-jump criterion with increments of Λ . For other phase-field fatigue models,

solely the specific choice for the variable to be extrapolated as well as the target increments $\Delta\bar{\Lambda}$ may be different. E.g. for models featuring cyclic plasticity [6, 61, 64], one choice could be to extrapolate the accumulated plastic strain during the skipped cycles. Furthermore, for phase-field fatigue models directly formulated in the cycle domain [60, 59], the proposed concept can be used as an adaptive cycle stepping algorithm.

Note also that, the extension to larger problems (e.g. in 3D) should not affect the efficiency of the method since the extra computational effort of the ACJ scales linearly with the problem size. This is related to the fact that only norms of arrays must be tracked to determine the cycle jump size and the explicit FD-based system state prediction can be fully vectorized.

4 Smeared crack tip tracking

In stage III, the proposed acceleration scheme relies on an accurate measurement of the crack growth rate to adaptively determine the cycle-jump size. In the following, we discuss why conventional crack tip tracking algorithms cannot be used, and propose the smeared crack length concept.

4.1 Issues of existing crack tip tracking algorithms

In a finite element (FE) computation, the simplest form of crack tip tracking is to identify the nodes with a phase-field value above a numerical threshold d_{th} as broken, and track the maximum (or minimum) of all broken nodal coordinates with respect to a given origin, as outlined e.g. in [26]. This means however that the direction of crack propagation must be known *a*

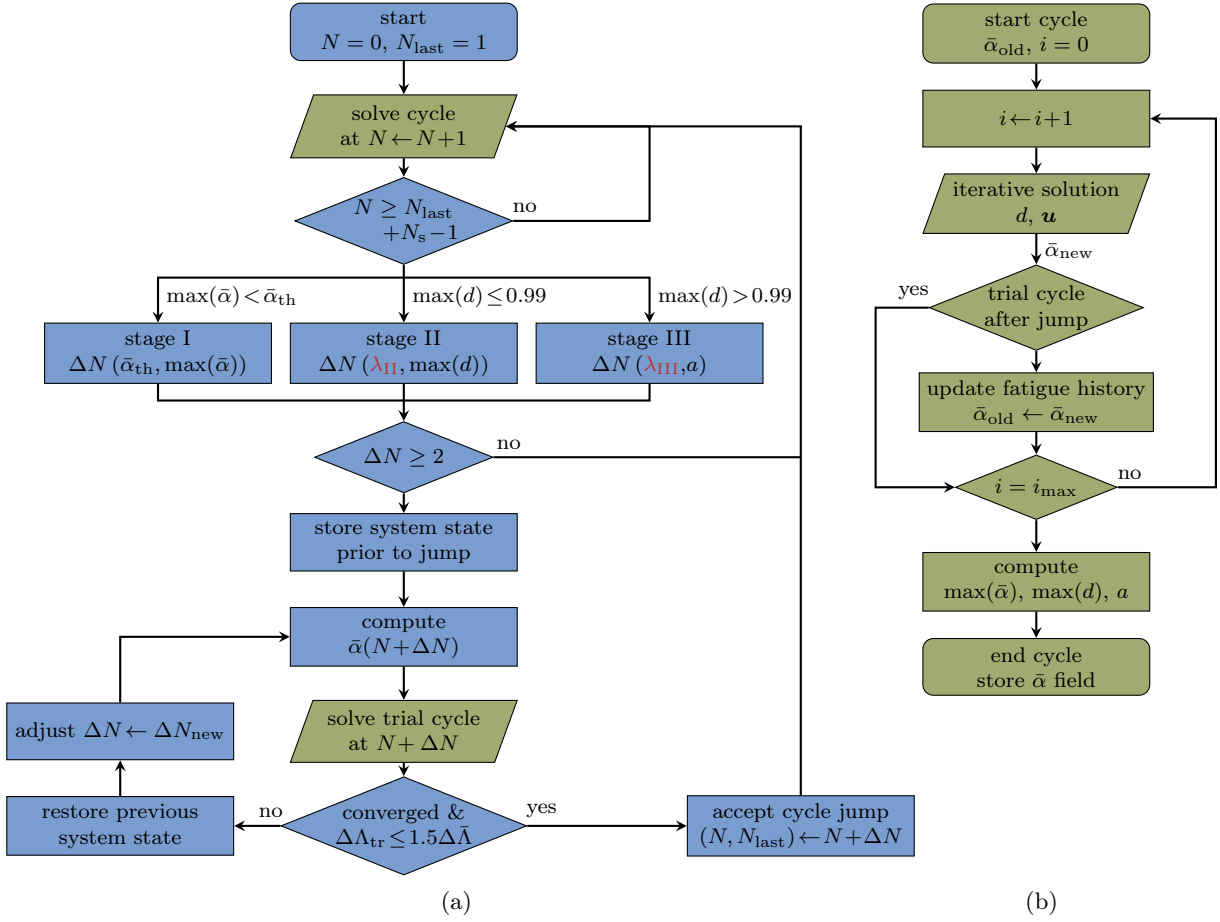


Figure 11: Flowchart illustrating the steps of the acceleration scheme (a) and of the solution of an individual cycle (b).

priori, while the minimal detectable crack growth is the discretization length h . This dependency on the spatial discretization is especially problematic for fatigue computations, where the crack growth rate may be significantly smaller than the discretization length, meaning that no crack propagation is observed for possibly thousands of cycles. More involved crack tip tracking strategies to automatically determine the direction of crack propagation or to incorporate branching could be an option, see e.g. [69], however they add computational cost.

4.2 Smeared crack length approach

The proposed cycle-jump scheme needs a crack tip tracking algorithm capable of detecting very small crack growth, without knowing the crack path *a priori*, while still being computationally efficient. To achieve this, we compute the crack length a by equating the integral of the numerically obtained phase-field solution $D_{\text{num}}(d)$ with the theoretical value obtained by integrating the optimal phase-field profile $D_{\text{opt}}(a, \ell)$,

i.e.

$$D_{\text{num}}(d) = D_{\text{opt}}(a, \ell). \quad (23)$$

To obtain $D_{\text{opt}}(a, \ell)$, for a 2D setting, we assume that the optimal phase-field profile is extruded along the crack axis, and that its half-profile is revolved around the crack tip, as illustrated in Fig. 12 exemplarily for the AT1 model. Hence, we split D_{opt} into contributions of the crack length D_{ext} and of the crack tip D_{tip} ,

$$D_{\text{opt}}(a, \ell) = D_{\text{ext}}(a, \ell) + k D_{\text{tip}}(\ell). \quad (24)$$

The factor $k \in \mathbb{N}$ allows to account for multiple crack tip contributions and must be set based on the expected number of crack tips. With the coordinate definition in Fig. 12, the two contributions read [22]

$$D_{\text{ext}}(a, \ell) = \int_{\xi_{\parallel}=0}^a \int_{\xi_{\perp}} d(\xi_{\perp}) d\xi_{\perp} d\xi_{\parallel} = a \begin{cases} \frac{4}{3}\ell & \text{AT1} \\ 2\ell & \text{AT2} \end{cases} \quad \text{and} \quad (25a)$$

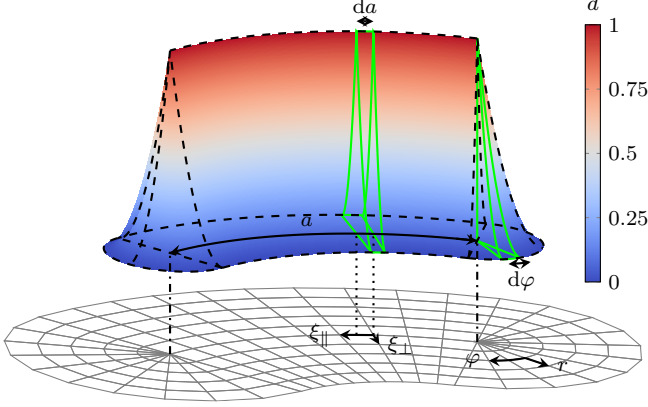


Figure 12: Crack tip and extension contributions of the optimal phase-field integral and local coordinate systems for their integration (exemplarily for the AT1 model).

$$D_{\text{tip}}(\ell) = \int_{\varphi=0}^{\pi} \int_r d(r, \varphi) r dr d\varphi = \pi \begin{cases} \frac{1}{3} \ell^2 & \text{AT1} \\ \ell^2 & \text{AT2} \end{cases}, \quad (25b)$$

Rearranging (23) for a yields

$$a = \frac{D_{\text{num}}(d) - k D_{\text{tip}}(\ell)}{D_{\text{ext}}(\ell)} = \begin{cases} \frac{D_{\text{num}}(d) - k \pi \frac{1}{3} \ell^2}{\frac{4}{3} \ell} & \text{AT1} \\ \frac{D_{\text{num}}(d) - k \pi \ell^2}{2 \ell} & \text{AT2} \end{cases}. \quad (26)$$

and the smeared crack growth rate reads

$$\dot{a} = \begin{cases} \frac{\dot{D}_{\text{num}}(d)}{\frac{4}{3} \ell} & \text{AT1} \\ \frac{\dot{D}_{\text{num}}(d)}{2 \ell} & \text{AT2} \end{cases}. \quad (27)$$

Crack branching or merging, or more generally multiple cracks are automatically dealt with. An extension to the 3D case to compute the crack surface is straightforward. In a numerical setting, the assumption of an optimal phase-field profile may not hold true due to the irreversibility condition and the discretization error. Their influence on the smeared crack length is investigated and corrected in Appendix A.1.

In a standard FE implementation, the computation of D_{num} involves numerical integration. An efficient integration is possible when assuming that the phase-field support is discretized uniformly. In this case, one can replace the numerical integration with the $L1$ -norm of the phase-field solution vector $\|\mathbf{d}\|_1$,

$$D_{\text{num}}(d) = J w \|\mathbf{d}\|_1 \quad \text{if} \quad h = \text{const.} \quad (28)$$

with a constant Jacobian J for the elements in the support, and sum of the numerical integration weights w . Both ways to compute the smeared crack length are compared and validated with conventional crack tip tracking algorithms in Appendix A.2.

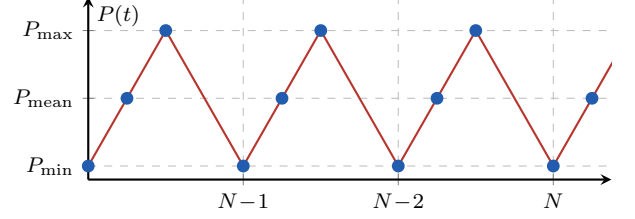


Figure 13: Discretization of the cyclic load applied (red curve) with multiple load steps (blue circles).

5 Numerical examples

In this section, the performance of the proposed adaptive acceleration scheme is demonstrated through numerical examples and compared with that of some other available acceleration schemes.

5.1 Numerical setup

For the numerical examples in this work, a standard FE procedure with a staggered solution scheme is adopted to solve the coupled problem. This means that the weak form of eqs. (5) and (6) is solved in an alternate fashion using an iterative Newton-Raphson scheme with a tolerance of $\text{TOL}_{\text{NR}} = 10^{-6}$ for the norm of the residual, until both residual norms fall below $\text{TOL}_{\text{stag}} = 10^{-4}$. All computations in the following are performed in the 2D setting and results are reported per unit thickness. The irreversibility of the phase field is enforced using the history-field approach [44], while different local dissipation functions and energy decompositions are adopted to assess the general applicability of the acceleration scheme. For the AT1 dissipation function, the recovery penalty proposed in [22] is used to ensure $d \geq 0$. Bilinear quadrilateral elements are used, while the meshes are locally refined in the areas of the expected crack. To discretize the loading cycles, the loading phases are resolved using multiple steps, while the intermediate load steps of the unloading phase are not resolved to save computational time. This can be done without loss of accuracy since the fatigue history variable only accumulates in the loading phases and the system behaves linearly during the unloading phases. Nonetheless, the final point of the unloading phase must be resolved such that the following loading phase is captured correctly, and since it is the reference point for the cycle-jump procedure. In this work, triangular load functions are considered with three load steps per cycle, that is two during loading and one during unloading as highlighted by the blue points in Fig. 13.

As clarified in Appendix A.2, the adoption of the smeared crack length approach introduces an approximation in the determination of the crack length. To

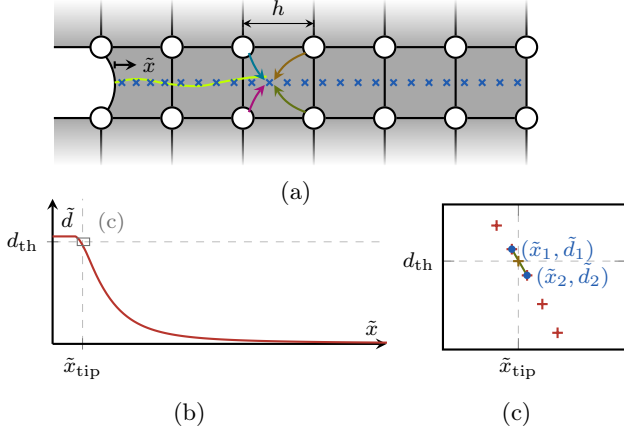


Figure 14: Steps to obtain the interpolated crack tip position, featuring the element-wise projection of the phase-field solution to the inter-nodal regime (a), the selection of relevant points of the projected phase field along a crack path coordinate $\tilde{d}(\tilde{x})$ (b), and the linear interpolation of the crack tip position \tilde{x}_{tip} (c).

avoid including such effect in the following comparisons, we adopt here a conventional crack tip tracking algorithm. To still detect crack length increments smaller than the discretization length (Section 4.1), we use an interpolated crack tip approach for specimens where the crack path is known *a priori* to obtain the crack growth rate curves. As illustrated in Fig. 14, we project the nodal phase-field solution onto a crack path coordinate \tilde{x} with the shape functions of the elements crossed by the crack (Fig. 14a). Based on the projected phase field along the crack path $\tilde{d}(\tilde{x})$, Fig. 14b, we can determine the position along the crack path where $\tilde{d}(\tilde{x}) = d_{th}$. This is done by linearly interpolating the projected phase-field values, as depicted in Fig. 14c. The crack growth rate is assessed at interpolated crack length increments of $\Delta a = \ell/2$.

5.2 Compact tension test

We consider a compact tension (CT) specimen with geometry and dimensions in Fig. 15a, assuming plane-stress conditions (however without explicitly enforcing $\sigma_{33} = 0$ as the phase field evolves, see [40] for more details). The test is performed in load control applying the boundary conditions in Fig. 15b. Following the parameters in Fig. 13, the load cycles have $P_{min} = 0$ N and P_{max} ranging between 50 N and 150 N to cover different fatigue regimes. We adopt the parameters in [11], namely Young's modulus $E = 6000$ MPa, Poisson's ratio $\nu = 0.22$, regularizing length $\ell = 0.2$ mm, and fracture toughness $\mathcal{G}_c = 2.28$ MPa mm leading to a critical stress intensity factor $K_{Ic} = 3.69$ MPa $\sqrt{\text{m}}$. Also, we compare the results for both the AT1 and AT2 local dissipation functions, we choose the spectral energy decomposition [45] and we set $\lambda_{II} = \lambda_{III}$ if not

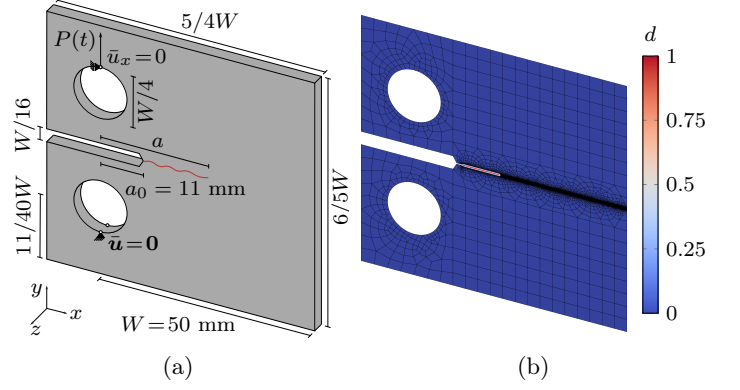


Figure 15: Geometry, boundary conditions (a) and finite element mesh showing the phase-field contour at an exemplary load step during fatigue crack propagation (b) for the CT test.

stated otherwise. For the fatigue degradation function (3) we set $\bar{\alpha}_{th} = 60$ N mm $^{-2}$ and $p = 2$. The mesh with 20736 bilinear quadrilateral elements and 20844 nodes is locally refined in the area of the expected crack path with $\ell/h \approx 5$, as depicted in Fig. 15b.

5.2.1 Speedup and accuracy

In Fig. 16, the predicted crack growth rates are presented at the load levels $P_{max} = 50$ to 150 N for the CT test, obtained with HF and accelerated computations. For the ACJ, we investigate also the role of the speedup parameters by comparing the results obtained with $\lambda_{II} = \lambda_{III} = 0.5, 1, 1.5$. We can observe an almost perfect overlap of the crack growth rate curve independently of the load applied or of the used speedup parameters $\lambda_{II,III}$. In particular, the ACJ is able to correctly reproduce the initial crack nucleation phase, the stable crack propagation (i.e., the Paris regime) and the final unstable failure stage (Fig. 16). The load level $P_{max} = 50$ N is the lowest one attainable with a HF computation within a reasonable amount of time, i.e., in about 8 days (7.5 days), yielding a fatigue life of $N_u = 27998$ cycles (27948 cycles) for the AT1 (AT2) model, which can still be considered as LCF regime. In contrast, the ACJ computation at the same load level takes about 13 hours (14 hours) for $\lambda_{II} = \lambda_{III} = 1$ and the AT1 (AT2) model, cutting the CPU time by 93 % (92 %) with of a deviation in terms of fatigue life (i.e., the total number of cycles until failure) of only 1.1 % (0.3 %). For the ACJ with $\lambda_{II} = \lambda_{III} = 1$, the number of resolved cycles is $N_r = 1045$ cycles, that is 3.7 % (1053 cycles, 3.8 %) of the total number of cycles. Similar considerations apply to the other load levels (Tab. 2), demonstrating that the ACJ approach is able to provide fast, yet accurate results. Tab. 2 reports CPU

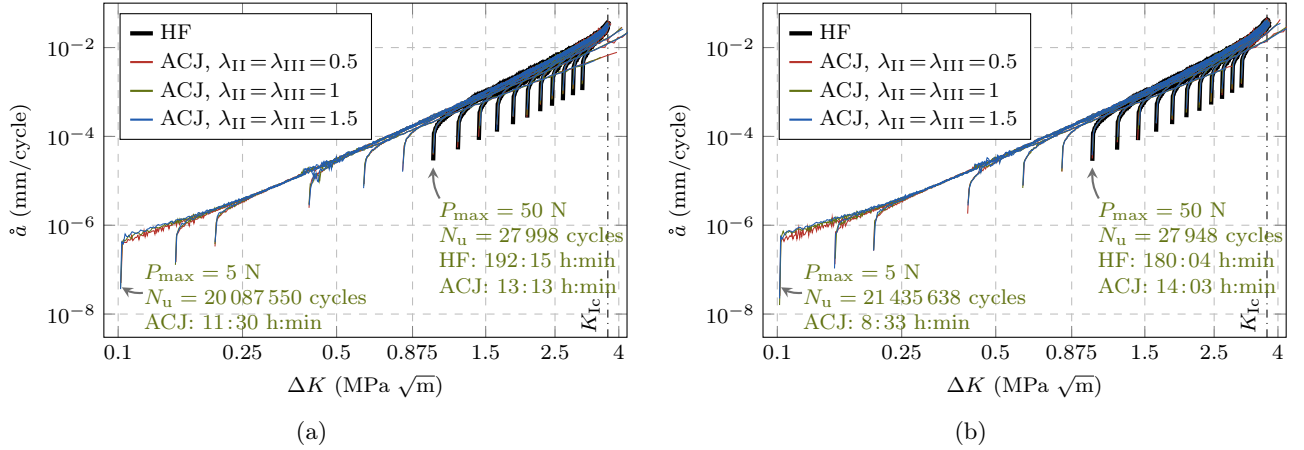


Figure 16: Comparison of crack growth rate curves for the CT test with the AT1 (a) and AT2 (b) model, as obtained from HF computations and the proposed ACJ scheme with different speedup factors. The HF-computed curves are limited to the load levels for which failure is reached within a computational time of two weeks (i.e., $P_{\max} = 50, 60, 70, 80, 90, 100, 110, 120, 130, 140, 150$ N). Additionally, the ACJ approach allows to compute the crack growth rate curve for the load levels $P_{\max} = 5, 7.5, 10, 15, 20, 30, 40$ N.

time, number of resolved cycles N_r and estimated fatigue life N_u , only for the AT1 model since the results for the AT2 model are very similar.

The proposed ACJ scheme allows to extend the study to HCF, whose computational cost is prohibitive for a HF computation. Fig. 16 shows the predicted crack growth rates for additional load levels down to $P_{\max} = 5$ N, for which a predicted fatigue life of around $2 \cdot 10^7$ cycles is obtained within less than a day. The small change of computational time when comparing the case $P_{\max} = 5$ N with $P_{\max} = 50$ N is due to the slow evolution rate of the system, which allows for larger jumps. For such long fatigue lives, some minor oscillations of the crack growth rate curve can be observed in the early stable crack propagation stage. For the lowest load levels in the VHCF regime, no distinctive unstable crack propagation branch of the crack growth rate curve can be observed anymore, and the branch of stable crack propagation (i.e., the Paris regime) appears to be slightly less steep. The details of the computations for $P_{\max} = 5, 7.5, 10, 15, 20, 30, 40$ of Fig. 16 are summarized in Tab. 3, again only for the AT1 model. We can observe that the computational time barely depends on the load level, while it is influenced by the speedup factors, and likewise for the number of resolved cycles, which is in line with the discussion in Section 3.4.4. For the lowest load level $P_{\max} = 5$ with $\lambda_{II,III} = 1.5$, only 1006 of the total $N_u = 19\,565\,228$ cycles are resolved (0.01 %) within only around 6 hours of computational time. It can be concluded that, in these fatigue regimes, the proposed acceleration scheme enables computations which are otherwise not feasible.

5.2.2 Comparison with other approaches

We now compare our ACJ scheme with other available approaches in terms of accuracy and speedup. In particular, we consider two alternatives to determine the cycle-jump size ΔN . In particular, we consider two alternatives to determine the cycle-jump size ΔN . Firstly, we use a fixed cycle jump (FCJ), where a jump with $\Delta N = \text{const.}$ is performed after each block of resolved cycles, where we choose sizes of $\Delta N = 100, 1000, 10000$ cycles. Secondly, we use the cycle jump based on a criterion on the extrapolation of $\bar{\alpha}$ proposed in [61], referred to as ECJ in the following, which determines the cycle-jump size as

$$\Delta N(N) = \min \left\{ q \cdot \min_{\mathbf{x} \in \Omega} \left\{ \frac{|\Delta \bar{\alpha}(\mathbf{x}, N)|}{|\Delta \bar{\alpha}(\mathbf{x}, N) - \Delta \bar{\alpha}(\mathbf{x}, N-1)|} \right\}, \Delta N_{\max} \right\} \quad (29)$$

$$\text{with } \Delta \bar{\alpha}(\mathbf{x}, N) = |\bar{\alpha}(\mathbf{x}, N) - \bar{\alpha}(\mathbf{x}, N-1)|.$$

Here q is a user-defined parameter governing the maximum relative deviation between the rate of the extrapolated quantity prior to and after the jump. As local variable to be extrapolated we use $\bar{\alpha}(\mathbf{x}, N)$ as well, and for a fair comparison, the extrapolation is performed using (8) and a set of N_s resolved cycles. Since in [61] no value for the user parameter is indicated, here $q = 1$ is used. Further, we added an upper limit for the jump extension ΔN_{\max} to avoid too optimistic cycle jumps and to increase the stability of the scheme in e.g. the very beginning or in the transition between the different stages of the computations. Since there is no

Table 2: Predicted fatigue life N_u , number of resolved cycles N_r and CPU time for the CT test comparing HF computations with the ACJ for different speedup parameters in the LCF regime (AT1 model).

P_{\max}	ACJ, $\lambda_{II} = \lambda_{III} = 0.5$			ACJ, $\lambda_{II} = \lambda_{III} = 1$			ACJ, $\lambda_{II} = \lambda_{III} = 1.5$		
	N_u	HF time (h:min)	N_u N_r time (h:min)	N_u N_r time (h:min)	N_u N_r time (h:min)	N_u N_r time (h:min)			
150	403 (100%)	8:17 (100%)	404 (+0.3%) 228 (56%) 5:35 (67%)	408 (+1%) 157 (38%) 3:26 (42%)	415 (+3%) 125 (30%) 2:39 (32%)				
140	600 (100%)	11:26 (100%)	604 (+0.7%) 318 (53%) 7:17 (64%)	606 (+1%) 209 (34%) 4:23 (38%)	615 (+3%) 160 (26%) 3:13 (28%)				
130	867 (100%)	14:48 (100%)	870 (+0.4%) 417 (48%) 8:34 (58%)	874 (+0.8%) 272 (31%) 5:22 (36%)	887 (+2%) 206 (23%) 4:06 (28%)				
120	1237 (100%)	20:36 (100%)	1241 (+0.3%) 528 (43%) 9:52 (48%)	1248 (+0.9%) 339 (27%) 6:21 (31%)	1269 (+3%) 252 (20%) 4:43 (23%)				
110	1781 (100%)	25:34 (100%)	1788 (+0.4%) 671 (38%) 13:09 (51%)	1804 (+1%) 421 (23%) 8:26 (33%)	1828 (+3%) 314 (17%) 6:22 (25%)				
100	2582 (100%)	35:26 (100%)	2589 (+0.3%) 826 (32%) 15:15 (43%)	2601 (+0.7%) 511 (20%) 9:27 (27%)	2629 (+2%) 370 (14%) 7:22 (21%)				
90	3815 (100%)	47:17 (100%)	3824 (+0.2%) 1003 (26%) 16:17 (34%)	3860 (+1%) 602 (16%) 10:12 (22%)	3888 (+2%) 433 (11%) 7:54 (17%)				
80	5801 (100%)	67:14 (100%)	5815 (+0.2%) 1199 (21%) 17:53 (27%)	5875 (+1%) 701 (12%) 11:23 (17%)	5914 (+2%) 499 (8%) 8:05 (12%)				
70	9187 (100%)	97:44 (100%)	9212 (+0.3%) 1417 (15%) 19:43 (20%)	9256 (+0.8%) 805 (9%) 11:45 (12%)	9358 (+2%) 565 (6%) 8:22 (9%)				
60	15405 (100%)	121:35 (100%)	15450 (+0.3%) 1650 (11%) 21:21 (18%)	15558 (+1%) 921 (6%) 15:20 (13%)	15726 (+2%) 637 (4%) 9:06 (7%)				
50	27998 (100%)	192:15 (100%)	28084 (+0.3%) 1912 (7%) 22:38 (12%)	28293 (+1%) 1045 (4%) 13:13 (7%)	28551 (+2%) 713 (3%) 9:31 (5%)				

Table 3: Predicted fatigue life N_u , number of resolved cycles N_r and CPU time for the CT test obtained with the ACJ for different speedup parameters in the HCF regime with no reference results from HF computations available (AT1 model).

P_{\max}	ACJ, $\lambda_{II} = \lambda_{III} = 0.5$			ACJ, $\lambda_{II} = \lambda_{III} = 1$			ACJ, $\lambda_{II} = \lambda_{III} = 1.5$		
	N_u	N_r	time (h:min)	N_u	N_r	time (h:min)	N_u	N_r	time (h:min)
40	57513	2197	24:20	57836	1171	13:47	58511	793	9:30
30	142453	2504	24:13	142845	1305	13:40	145023	881	9:36
20	497044	2837	23:18	499065	1459	12:28	510366	973	8:36
15	1207717	3025	22:39	1208843	1536	12:27	1219572	1029	9:12
10	3859061	3189	20:12	3781558	1602	10:32	3776734	1058	8:08
7.5	8161776	3200	24:07	7835092	1592	10:25	7640258	1054	6:57
5	21595566	3114	18:47	20087550	1509	11:30	19565228	1006	6:06

possibility to determine *a priori* a feasible limit, we use $\Delta N_{\max} = 1000, 10000$ cycles. To allow for a fair comparison, all the approaches are implemented within the same code, while the analyses are performed on comparable hardware. Only the computations which reach a stress intensity factor amplitude of at least 70 % of K_{Ic} are considered in the comparison; the runs during which the computations stop prior to that point due to numerical issues are not considered as valid.

To provide a more insightful evaluation of the performance of the approaches, we introduce first the fatigue life prediction error ϵ_N as

$$\epsilon_N := \frac{N_u}{N_{u, \text{HF}}} - 1 \quad (30)$$

to compare the accuracy of the accelerated computations to the HF computations wherever possible. Secondly, the speedup is quantified in terms of CPU time ω_{CPU} as

$$\omega_{\text{CPU}} := \frac{\text{CPU time}}{\text{CPU time}_{\text{HF}}} - 1, \quad (31)$$

and finally, since for peak loads $P_{\max} < 50$ N, no HF computation is available, the speedup is obtained in terms of resolved cycles N_r for the estimated fatigue life N_u as

$$\omega_N = \frac{N_u}{N_r}. \quad (32)$$

For the ACJ, the FCJ, and the ECJ approach, the accuracy in terms of ϵ_N and the speedup in terms of ω_{CPU} in comparison to the HF computations are plotted in Figs. 17a and 17b, respectively.

First, we note that some data points of the FCJ and ECJ approach are missing due to the impossibility to reach convergence and hence 70 % of K_{Ic} after a too optimistic cycle jump, either within the Newton-Raphson iterative solution of the equilibrium or damage equation, or within the staggered scheme within the allotted maximum number of iterations (250 for each). This is the case for all the FCJ computations with $\Delta N = 10000$ and almost all with $\Delta N = 1000$ cycles, highlighting the lack of robustness of this approach and the critical role played by the choice of ΔN . $\Delta N = 100$ cycles seems to be the most suitable choice for an LCF regime, while the obtained speedup in terms ω_{CPU} is limited (Fig. 17b), and the

error ϵ_N is quite high, reaching up to about 77 % (Fig. 17a). Considering the ECJ, none of the tested ΔN_{\max} values ensures convergence for all test cases, highlighting the key role of this parameter for which no estimate is available. In particular, when higher values of ΔN_{\max} are selected, convergence issues are observed in the LCF regimes along with higher fatigue life estimation errors ϵ_N (Fig. 17a), while for low ΔN_{\max} values, a small speedup is obtained in the HCF regime. Thus, these approaches achieve either a good speedup or a good accuracy with an appropriate estimate for their parameters, but not both, while numerical issues are encountered with a bad estimate for their parameters. Conversely, the proposed approach reaches convergence for any of the tested speedup parameters $\lambda_{II,III}$ while keeping the error ϵ_N consistently below around 3 %, clearly depending on the choice of $\lambda_{II,III}$. Moreover, the obtained speedup is always higher and growing at an increasing rate towards the HCF regime. Comparing Fig. 17a (ϵ_N) with Fig. 17b (ω_{CPU}) offers a further confirmation of the role of $\lambda_{II,III}$ as parameters governing the trade-off between accuracy and efficiency.

Extending the performance analysis to the HCF regime with the additional load levels by evaluating ω_N in Fig. 18, the same conclusions can be drawn. In particular, Fig. 18a shows ω_N for different load levels, while Fig. 18b gives ω_N as a function of the total fatigue life. As observed before, some data points are missing for the FCJ and ECJ either due to the mentioned numerical issues, or since the speedup obtained was too small such that the computation did not reach the final stage within a week of computational time. In contrast, the proposed ACJ consistently reaches the final stage of the fatigue life even for the lowest load levels, showing a robust behavior in dependency of the speedup factors. Also, the value of ω_N increases for decreasing P_{\max} until reaching, for $\lambda_{II,III} = 1$, a speedup of more than four orders of magnitude, namely $\omega_N = 1.3 \cdot 10^4$ ($1.4 \cdot 10^4$) for the AT1 (AT2) model. This means that on average, one cycle every 13312 (14038) cycles needs to be resolved. Similar observations can be made for the analysis with $\lambda_{II,III} < 1$ ($\lambda_{II,III} > 1$) for which a lower (higher) speedup is obtained in spite of the negligible variation of the crack growth rate curve (Fig. 16) and fatigue life (Tab. 3). For speedup factors of $\lambda_{II,III} = 1.5$ even higher values up to almost $\omega_N = 2 \cdot 10^4$ are obtained.

5.2.3 Behavior in different stages and fatigue life regimes

Next, we analyze the behavior of the proposed ACJ scheme within the different stages of the fatigue life. Fig. 19 illustrates for stage I the extension of the cycle

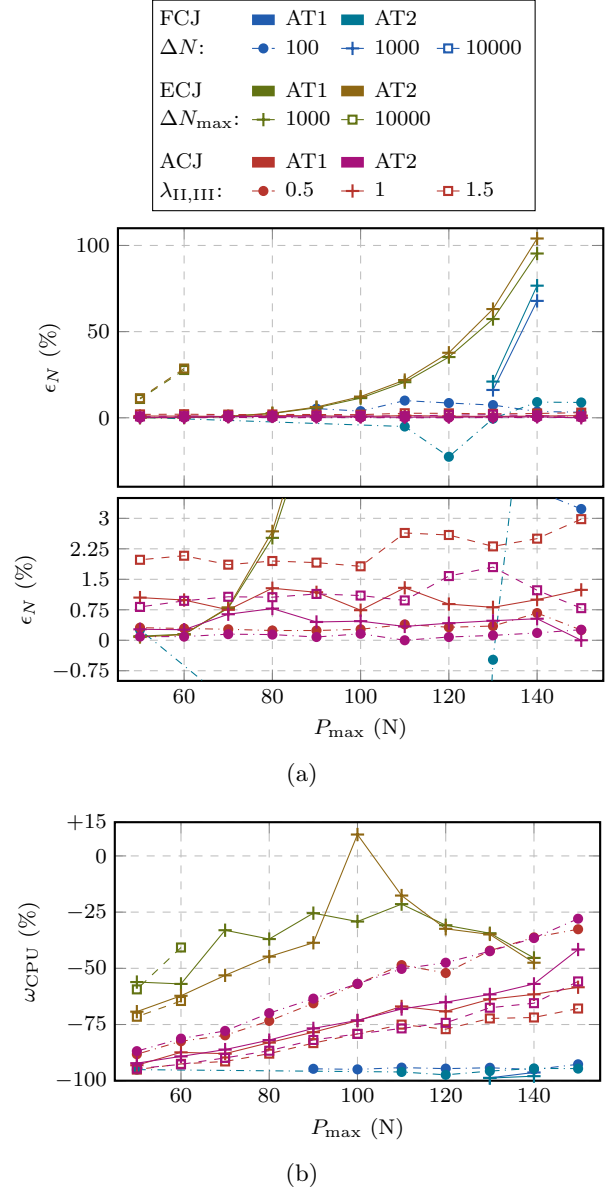


Figure 17: Comparison of the FCJ, ECJ and ACJ approaches to HF computations in terms of accuracy ϵ_N (a) and speedup ω_{CPU} (b) for the CT test in the LCF regime.

jump as a function of the maximum applied load P_{\max} for the AT1 model, since for the AT2 model, the same conclusions can be drawn. The black data points indicate the cycle at which the fatigue threshold $\bar{\alpha}_{th}$ is met for the first time $N|_{\bar{\alpha}=\bar{\alpha}_{th}}$. The first data point at N_s indicates the start of the cycle jump while the second data point represents the cycle to which the algorithm jumps, which is either slightly below $N|_{\bar{\alpha}=\bar{\alpha}_{th}}$ or matching it exactly. At high load levels ($P_{\max} = 150$ N), this allows for a small jump of only 2 cycles after the first N_s resolved cycles, while the cycle-jump size significantly increases as the applied load decreases. This applies to both AT1 and AT2.

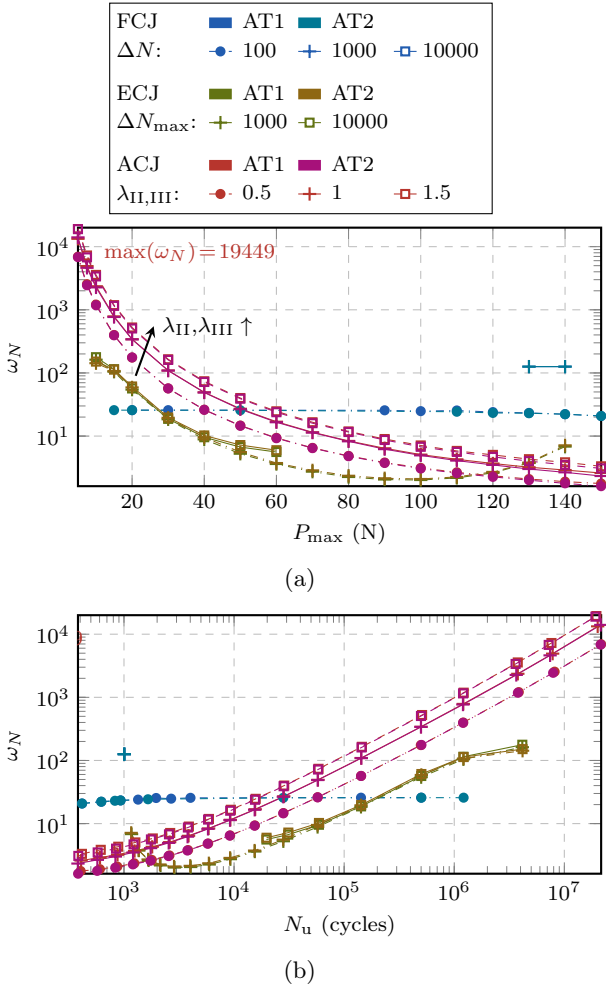


Figure 18: Comparison between the FCJ, ECJ and ACJ approaches in terms of speedup ω_N for different load levels (a) and number of cycles until failure (b) for the CT test.

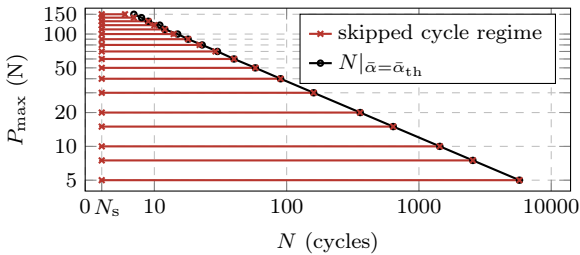


Figure 19: Stage I cycle-jump size for the CT test and comparison with the stage extension in terms of number of cycles obtained adopting the AT1 model.

For the analysis of stage II and stage III, we select three load levels representative of different fatigue regimes, namely the LCF regime at $P_{\max} = 120$ N, an intermediate regime at $P_{\max} = 30$ N, and the HCF regime at $P_{\max} = 10$ N. Figs. 20 (a,c,e) and 20 (b,d,f) show the performed cycle jumps ΔN at these load levels during stage II and stage III, respectively. The

proposed algorithm performs well for these different regimes characterized by a fatigue life N_u ranging from 10^3 cycles to more than 10^6 cycles. It is evident that the extension of the jumps is larger at the beginning of both stage II and III due to the lower evolution rate of the system and reaches up to more than 10^2 , 10^4 and 10^5 cycles respectively for $P_{\max} = 120$ N, 30 N and 10 N. The amount of jumped cycles then gradually decreases as the rate of change of the global control quantity Λ increases, until reaching the minimum jump size $\Delta N = 2$ at the end of each stage. This is the case even in the HCF regime, where the largest cycle jump is 375392 cycles. As demonstrated by Figs. 21 (a-f), this change of the jump size is needed to ensure that the variation of the global control variable during a jump $\Delta\Lambda$ remains close to the imposed value $\Delta\bar{\Lambda}$, highlighting the reliability of the proposed cycle-jump criterion. Note that at the very end of stages II and III, the system evolves so quickly that the cycle-jump criterion would give $\Delta N < 2$, therefore the algorithm reverts back to a HF computation as detailed in Section 3.3.3. For the case illustrated here, rejecting a cycle jump which encountered convergence issues or gave a too large $\Delta\Lambda$ during the trial cycle (Section 3.5) is limited to either the beginning or the end of a stage, as indicated with the orange data points in Figs. 20 and 21.

Fig. 21 clarifies also the role of the speedup parameters λ_{II} and λ_{III} , which modulate the target value $\Delta\bar{\Lambda}$ and hence, reduce or increase the jump size. An increase of $\lambda_{II,III} > 1$ leads to less computational effort, but too optimistic cycle jumps needing correction are more frequent. Based on the performed computations, we suggest to keep $\lambda_{II,III} \leq 1.5$ to preserve the robustness and accuracy of the results. Also, the proposed ACJ algorithm behaves similarly for both AT1 and AT2 dissipation functions without modifying the target values $\Delta\bar{\Lambda}$, and for any investigated value of λ_{II} and λ_{III} , further confirming the robustness of the method.

Tab. 4 gives a quantitative comparison of the performed cycle jumps in the different stages, only for the AT1 model since the results for the AT2 model are very similar. Clearly, most of the CPU time is spent in stage III, while stage I takes the smallest time.

In Fig. 22 we compare the estimate for the number of cycles which need to be computed $N_{r,est}$ (Section 3.4.4) with the number of actually resolved cycles N_r . At the higher load levels, the $N_r/N_{r,est}$ ratio is around 0.5, meaning that only about half of the estimated number of HF cycles are actually computed. This difference is due to the fact that, in the LCF regime, the system experiences a non-negligible evolution also during the HF computed cycles, which is neglected in

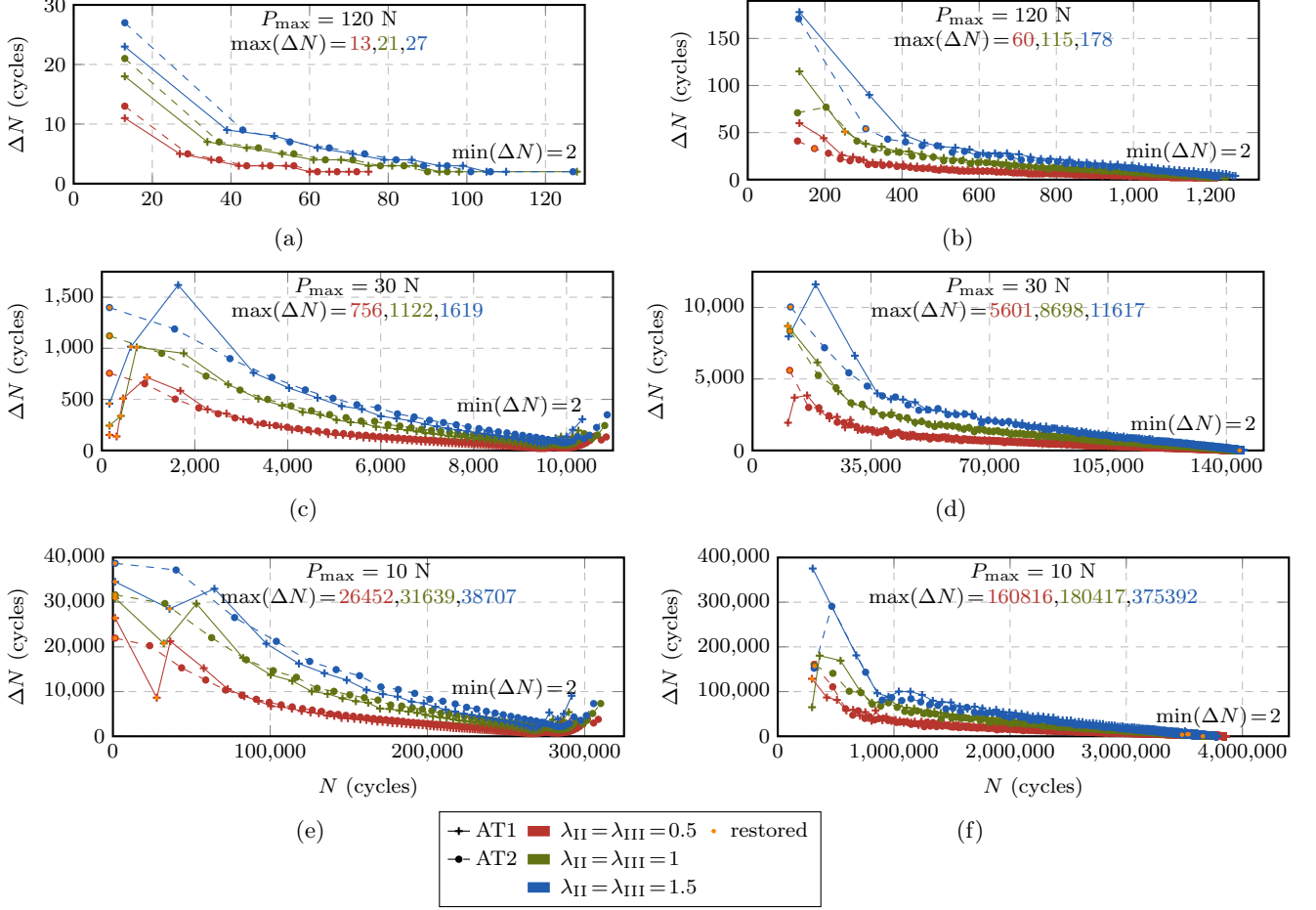


Figure 20: Size of the performed cycle jumps throughout the fatigue life in stage II (a,c,e) and in stage III (b,d,f) at selected load levels $P_{\max} = 10, 30, 120$ N for the CT test. The points are connected by lines for better visibility.

Table 4: Comparison of the different stages in terms of cycle-jump sizes, number of resolved cycles and percentage of total CPU time spent within each of the three stage for the CT test (AT1 model).

P_{\max}	$\lambda_{II,III}$	N_u	ΔN	stage I		# jumps	stage II		# jumps	stage III	
				$N_{r,I}$	time share (%)		$N_{r,II}$	time share (%)		$N_{r,III}$	time share (%)
10	0.5	3859061	1434	5	0.03%	101	403	3%	693	2781	97%
	1	3781558	1434	5	0.06%	52	207	3%	347	1390	97%
	1.5	3776734	1434	5	0.08%	36	143	3%	226	910	97%
30	0.5	142453	156	5	0.03%	98	391	3%	522	2108	97%
	1	142845	156	5	0.05%	52	207	4%	272	1093	96%
	1.5	145023	156	5	0.07%	36	143	3%	182	733	97%
120	0.5	1241	6	6	0.1%	10	95	4%	102	427	96%
	1	1248	6	6	0.2%	12	75	6%	65	258	93%
	1.5	1269	6	6	0.3%	11	64	8%	46	182	92%

(21). The higher the fatigue life, the more the ratio $N_r/N_{r,est}$ tends towards one, which means that the algorithm is performing as expected, due to the obtained increments $\Delta\bar{N}$ being close to the target value.

Finally, we address the accuracy of the system state prediction, that is the extrapolation of $\bar{\alpha}$. To estimate it, we compare the computed and extrapolated $\bar{\alpha}(\mathbf{x}, N)$ for the $N_s - 1$ cycles following a cycle jump, i.e. for the

cycles needed to perform the subsequent jump excluding the trial cycle, as illustrated in Fig. 23a. For these cycles, we use (8) to compute an average error

$$\epsilon_{\bar{\alpha}}(\mathbf{x}, N) = \frac{1}{N_s - 1} \sum_{i=1}^{N_s - 1} \frac{\bar{\alpha}^*(\mathbf{x}, N + \Delta N + i) - \bar{\alpha}(\mathbf{x}, N + \Delta N + i)}{\bar{\alpha}(\mathbf{x}, N + \Delta N + i)} \quad (33)$$

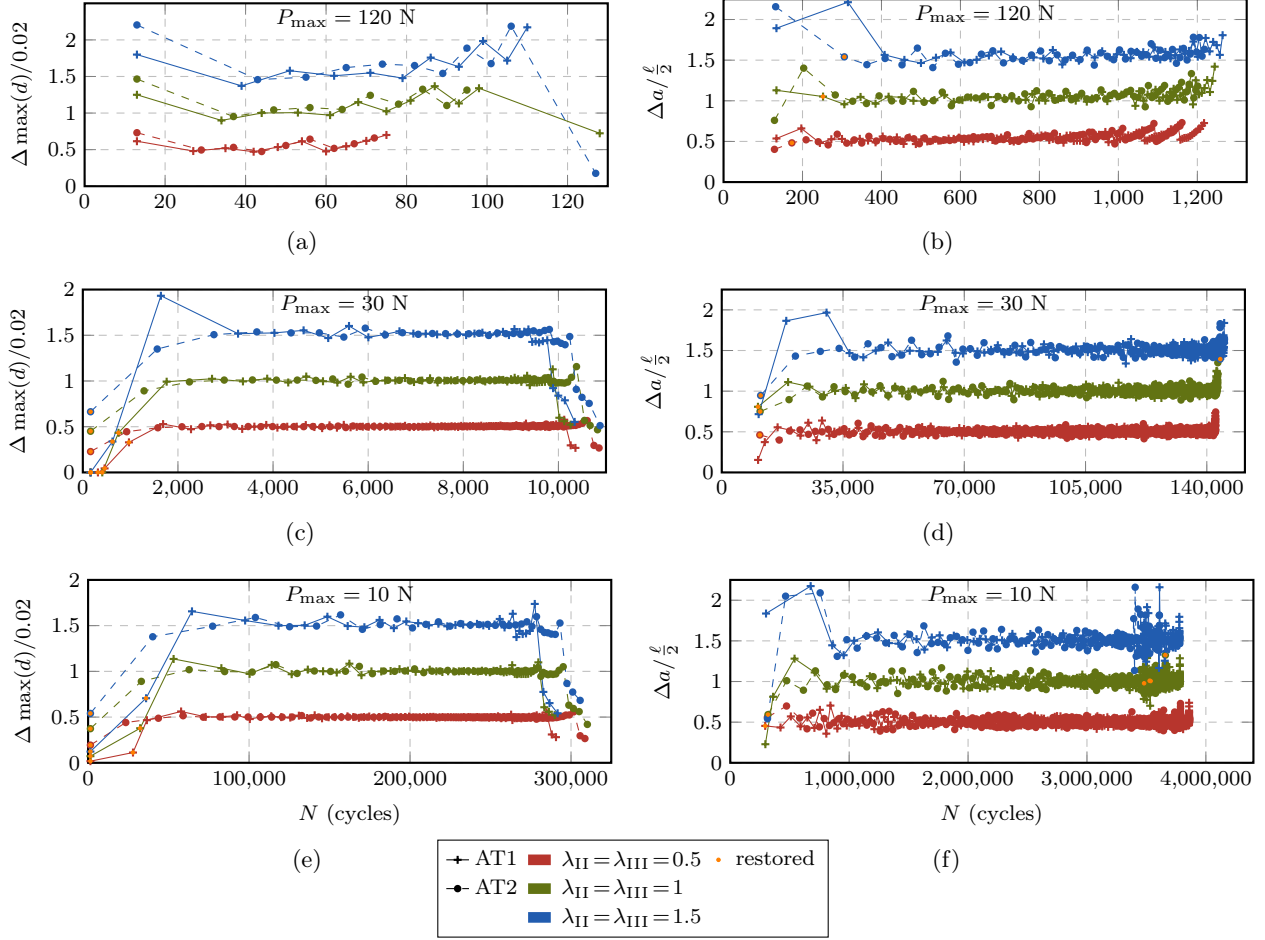


Figure 21: Obtained increments of Λ during the performed cycle jumps in stage II (a,c,e) and in stage III (b,d,f) at selected load levels $P_{\max} = 10, 30, 120$ N for the CT test. The points are connected by lines for better visibility.

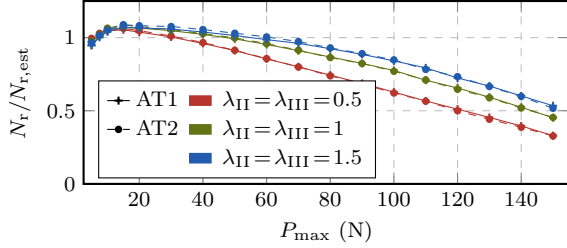


Figure 22: Comparison between the actual number of resolved cycles N_r and the estimate obtained using (21) for the CT test.

Figs. 23b and 23c show the contour plot of $\epsilon_{\bar{\alpha}}(\mathbf{x})$ for a representative cycle jump within stage II and stage III, respectively. We adopt $P_{\max} = 120$ N since it exhibits the largest errors, but we obtain similar results also at other load levels. Clearly, the prediction error is localized around the notch in stage II or the crack tip in stage III. Crack propagation leads to a relocation of the zone with dominant fatigue effect, meaning that the FD-based prediction of $\bar{\alpha}$ leads to areas of under- and overestimation, as evident e.g. in Fig. 23c.

Fig. 24 shows the evolution of the L_2 -norm of the estimated prediction error field $\|\epsilon_{\bar{\alpha}}\|_2$ at the three representative load levels. Stage I and II cycle jumps exhibit smaller prediction errors than stage III cycle jumps, which we attribute to the relocation of the crack tip with crack propagation. Only towards the end of the fatigue life close to N_u , we can observe a significant increase of the prediction error, which is due to the strongly non-linear behavior of the system in that stage. However, the errors within each individual stage tend to be of the same order of magnitude, despite the very different cycle-jump sizes. I.e., the cycle jumps in beginning of stage III at the lowest load level of more than $\Delta N \approx 10^5$ cycles lead to a similar prediction error as a cycle jump towards the end of this stage of $\Delta N = 2$ cycles. This ultimately proves that a cycle-jump size based on the crack growth (or $\max(d(\mathbf{x}))$) obtains stable prediction errors throughout the fatigue life, which was the original motivation for the cycle-jump criterion. Further, we can observe that larger speedup factors $\lambda_{II,III}$ clearly yield a higher

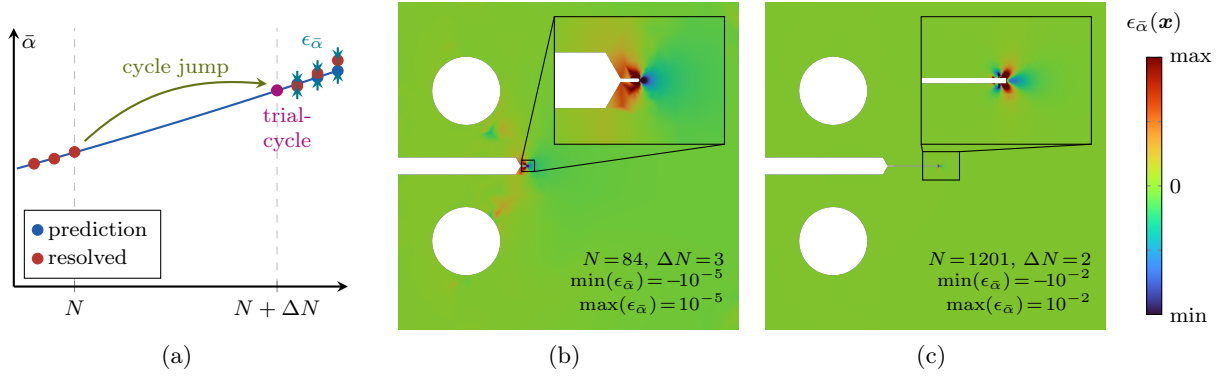


Figure 23: Approach to obtain an estimation of the prediction error (a) as well as representative prediction error field for a cycle jump in stage II (b) and stage III (c), where elements with $d \geq 0.95$ are hidden to indicate the crack.

prediction error, in line with the previous explanations. Finally, the AT1 and AT2 models yield very similar values for the prediction errors. We remark that the estimation of the local state prediction error is obtained by post-processing the obtained data and is not used to modify the jump extension. Although the checks on the accuracy of the prediction of the global quantities performed during the trial cycle (Section 3.5 and (22)) seem to be sufficient to guarantee a good accuracy, the introduction of a local error estimate can be a possibility to further improve the proposed ACJ.

5.3 Perforated plate test

Next, a more complex geometry is tested to evaluate the proposed acceleration scheme for multiple cracks nucleating at different instants and propagating at different rates. We use a setup similar to the one in [48], illustrated in Fig. 25a. A plate with 23 randomly distributed holes under plane-strain conditions is subjected to a prescribed compressive cyclic displacement on the upper edge, $\bar{u}_y(t)$, with $\bar{u}_{y,\max} = 0$ mm and $\bar{u}_{y,\min} = -2.5 \cdot 10^{-4}$, $-5 \cdot 10^{-4}$, $-6.25 \cdot 10^{-4}$, $-7.5 \cdot 10^{-4}$ mm. The adopted parameters are taken from [11], namely $E = 12000$ MPa, $\nu = 0.22$, $\mathcal{G}_c = 0.0014$ MPa mm and $\ell = 0.018$ mm. Also, we choose the AT2 model and the no-tension energy decomposition [20], while we set $\bar{\alpha}_{\text{th}} = 0.00648$ N mm $^{-2}$ and $p = 2$ for the fatigue degradation function. The mesh, shown in Fig. 25b, features 121831 bilinear quadrilateral elements and 123931 nodes, leading to $\ell/h \approx 3$ in the whole domain. For this test, we use six load steps per cycle, that is five during loading and one during unloading. The challenge in this case is the presence of multiple cracks that nucleate at different cycles and propagate at different rates due to the randomness of the hole positions. To show that the ACJ procedure is able to deal with this complexity without any modifications, again $\lambda_{\text{II}} = \lambda_{\text{III}} = 0.5, 1, 1.5$ are used for

the computations. Since for this specific setup the definition of the failure point is not straightforward, all results presented here are obtained by means of a total computation wall time of 14 days.

Fig. 26 compares the total crack length, as measured by the smeared crack length concept (now setting the expected crack tip number to $k = 23^1$), for the four different load levels. Evidently, the curves virtually coincide, while only the final predicted crack length is slightly overestimated by the proposed acceleration scheme, depending on the chosen speedup parameters. The jumps in the smeared crack length indicate either the nucleation of new cracks or the merging of propagating cracks, which the ACJ scheme can resolve with virtually no deviation from the HF computations. Despite this negligible difference, all of the ACJ computations reach a significantly higher cycle count in the 14 days of computation. This is especially evident at the lowest load amplitude with $\bar{u}_{y,\min} = -2.5 \cdot 10^{-4}$ mm (Fig. 26d), where the ACJ computation with $\lambda_{\text{II,III}} = 1.5$ reaches almost 220 000 cycles, in contrast to the HF computation which reaches around 30 000 cycles.

In this case, to compare the accelerated and HF results we consider the cycle N_{co} associated to the crack length a_{co} which the HF computations could obtain within two weeks of computational time. Tab. 5 gives a comparison in terms of N_{co} , number of resolved cycles N_r and CPU time for the different speedup factors. All the parameter combinations achieve an error of N_{co} below around 3 %, while only computing a small fraction of the total number of cycles. At the highest load amplitude, the system evolution is so quick that almost no

¹Note that the value used here for k is a rough estimation of the expected number of crack tips, since in this case not all the cracks nucleate at the same instant and not each hole triggers two cracks. This approximation, however, does not influence significantly the results because of two reasons. First, we compute crack increments and, second, the contribution due to the crack extension is much larger than the tip one.

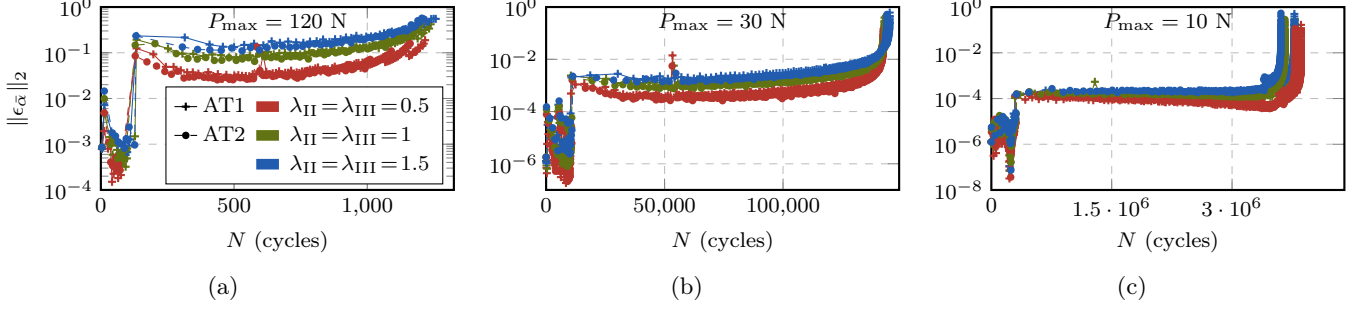


Figure 24: L_2 -norm of the estimated prediction error throughout the fatigue life for the CT test at different representative load levels (a-c).

Table 5: Number of cycles associated to the crack length attained by the HF computation within two weeks N_{co} , number of resolved cycles N_r and CPU time comparing HF with ACJ computations for the perforated plate test.

$\bar{u}_{y, \min}$	HF		ACJ, $\lambda_{II} = \lambda_{III} = 0.5$			ACJ, $\lambda_{II} = \lambda_{III} = 1$			ACJ, $\lambda_{II} = \lambda_{III} = 1.5$		
	N_{co}	time (h:min)	N_{co}	N_r	time (h:min)	N_{co}	N_r	time (h:min)	N_{co}	N_r	time (h:min)
-7.5	8487	330:42	8488	3754	242:23	8493	2300	168:57	8475	1652	108:37
$\cdot 10^{-4}$	(100%)	(100%)	(+0.01%)	(44.23%)	(73.3%)	(+0.07%)	(27.08%)	(51.09%)	(-0.14%)	(19.49%)	(32.84%)
-6.25	10679	329:13	10673	2977	193:37	10672	1708	131:48	10690	1207	106:39
$\cdot 10^{-4}$	(100%)	(100%)	(-0.06%)	(27.89%)	(58.82%)	(-0.07%)	(16.0%)	(40.04%)	(+0.10%)	(11.29%)	(32.4%)
-5	16583	326:51	16582	2592	136:52	16610	1378	63:20	16574	937	50:45
$\cdot 10^{-4}$	(100%)	(100%)	(-0.01%)	(15.63%)	(41.88%)	(-0.16%)	(8.3%)	(19.38%)	(-0.05%)	(5.65%)	(15.53%)
-2.5	30603	328:27	30001	568	9:32	29598	288	3:38	29323	204	2:46
$\cdot 10^{-4}$	(100%)	(100%)	(-1.97%)	(1.89%)	(+2.9%)	(-3.28%)	(0.97%)	(1.11%)	(-4.18%)	(0.7%)	(0.84%)

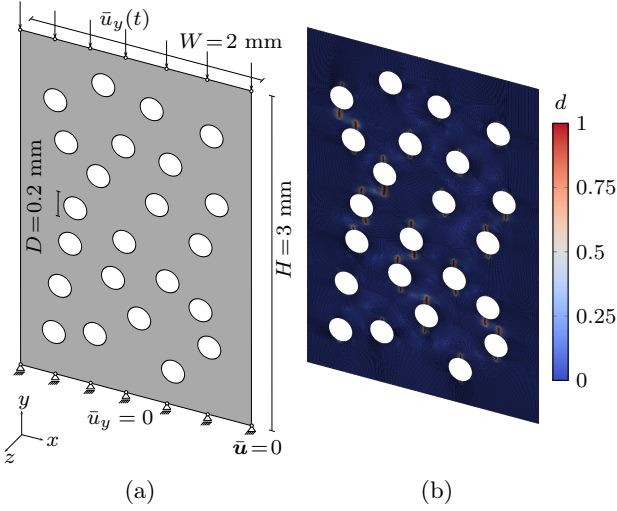


Figure 25: Geometry and boundary conditions (a) as well as FE mesh showing the phase-field contour at an exemplary cycle during the stage of fatigue crack propagation (b) for the perforated plate test.

cycle can be jumped, while for the lowest load level we notice a high speedup. For $\bar{u}_{y, \min} = -2.5 \cdot 10^{-4}$ mm, the ACJ with $\lambda_{II, III} = 1.5$ reaches the reference point of the HF computations within less than three hours of computational time (less than one percent of the HF time), while resolving only 204 cycles (0.7 %). Continuing after this reference point, it reaches 217 864 cycles

by resolving only 2033 cycles (0.93%) within around 14 days of computational time.

Next, Fig. 27 shows the performed cycle jumps throughout the fatigue life $\Delta N(N)$ as well as the increments of Λ during the jumps in stage II and stage III at $\bar{u}_{y, \min} = -2.5 \cdot 10^{-4}$ mm. In comparison to samples with a single crack tip, stronger oscillations are observed, however the target increments $\Delta \max(d)$ and Δa are still around the target value $\Delta \bar{\Lambda}$. As indicated with the orange points, the rejection of a cycle jump with too large $\Delta \Lambda$ or not converging occurs slightly more often than for the single-crack case, but is still very limited.

Finally, Fig. 28 shows the CPU time as a function of the cycle count N for the lowest load amplitude with $\bar{u}_{y, \max} = -2.5 \cdot 10^{-4}$ mm. The different slope of the curves for the HF and the ACJ computations with different speedup parameters clearly demonstrates the obtained speedup. While the HF computations show an almost linear correlation between computational time and cycle count, the ACJ results comprise regions where the computations appear to be much slower (at around 150 000 cycles). This is due to a strongly nonlinear and hence barely predictable evolution of the system during the nucleation of new cracks or the merging of existing cracks (Fig. 26d). There, the scheme provides reduced jump extensions (Fig. 27a) and it needs to restore cycles more frequently (Fig. 27c). This demonstrates the robustness of the proposed

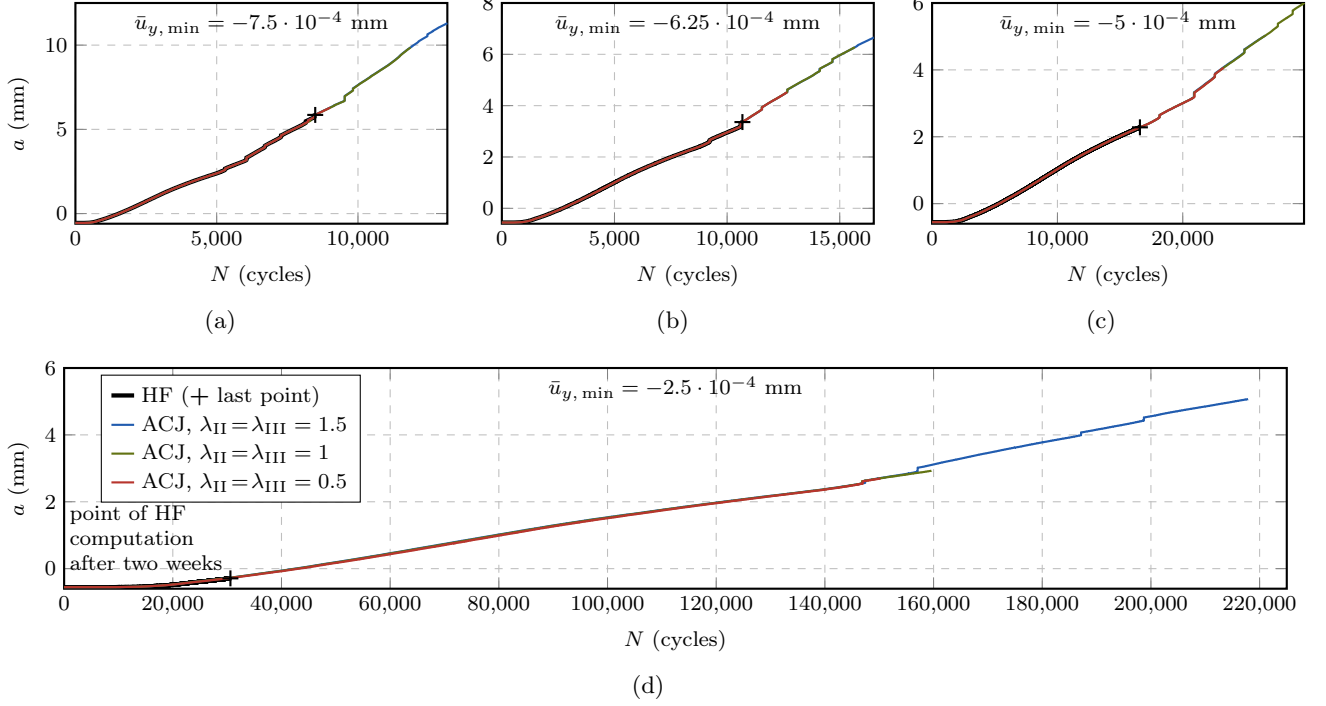


Figure 26: Comparison between the HF- and ACJ-computed total crack length as recorded by the smeared crack length approach for the perforated plate test with different maximum applied displacement magnitudes (a-d).

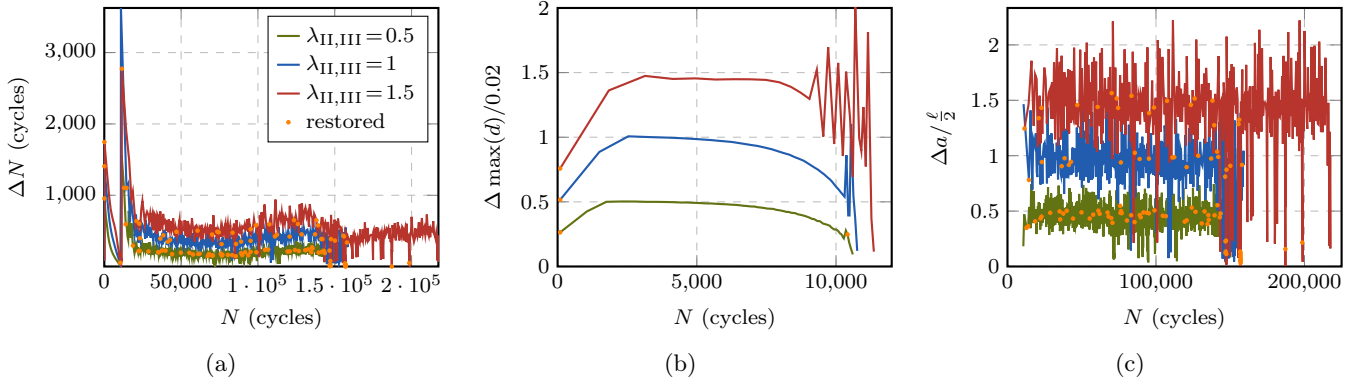


Figure 27: Comparison of the size of the performed cycle jumps ΔN (a), the obtained increments $\Delta \max(d)$ in stage II (b), and the obtained total crack length advancements Δa (c) for the perforated plate test with $\bar{u}_{y, \min} = -2.5 \cdot 10^{-4}$ mm. The data points are connected by lines for better visibility.

acceleration scheme and that it is capable of dealing with complex behaviors thanks to the definition of the global variables constraining the jump.

6 Conclusions

In this work, we propose an adaptive cycle-jump scheme to address the prohibitive computational cost of phase-field fatigue computations associated with predictions in the high cycle fatigue regime. We introduce a cycle-jump criterion which allows to determine

when a jump is feasible and how many cycles can be skipped based on a target increment of a global representative variable during the skipped cycles. For the definition of this global variable, the fatigue life is divided into (I) an initial stage before the fatigue effect is triggered, (II) the stage of fatigue crack nucleation, and (III) the crack propagation stage. For the third stage, to overcome issues of conventional crack tip tracking algorithms, we introduce the smeared crack length concept which is based on a comparison of the integral of the numerically obtained phase-field solution with the

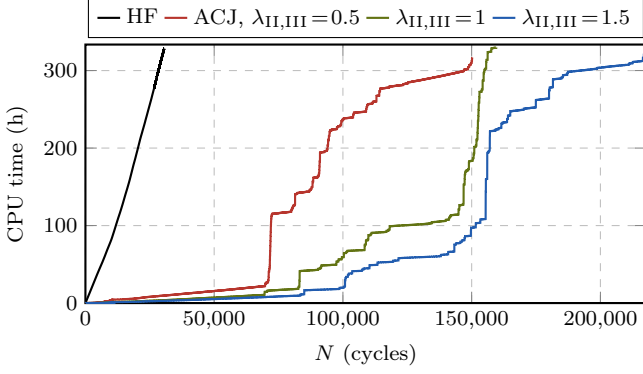


Figure 28: Comparison between the computational time as a function of the cycle count for the perforated plate test with $\bar{u}_{y, \min} = -2.5 \cdot 10^{-4}$ mm, for HF and ACJ computations with different speedup parameters.

integral of the optimal phase-field profile. Based on representative numerical tests, the following conclusions can be drawn:

- in contrast to existing acceleration techniques, the proposed approach shows a consistent behavior across different fatigue regimes as well as different loading and test scenarios;
- the number of cycles to be resolved depends only on a few parameters with clear meaning and can be estimated with good accuracy;
- the scheme automatically reverts back to a HF resolution of the cycles once fast system evolution is detected, thereby preventing loss of accuracy during critical stages of the fatigue life;
- errors below 3 % in terms of total fatigue life and a very good agreement of crack growth rate predictions can be achieved with a speedup factor of up to more than four orders of magnitude, which can directly be influenced by optional user parameters;
- thanks to the smeared crack length approach, the scheme is able to deal with complex phase-field fatigue computations such as with specimens including multiple cracks.

Ultimately, the proposed scheme enables phase-field fatigue computations in the HCF and VHCF regimes which were simply not possible without acceleration.

Supplementary information.

Acknowledgements. The help of Francesco Vicentini with the computation of the phase-field profiles during localization is gratefully acknowledged. We acknowledge funding from the Swiss National Science Foundation through Grant No. 200021-219407 ‘Phase-field modeling of fracture and fatigue: from rigorous theory to fast predictive simulations’. Jonas Heinzmann acknowledges funding of the German Academic

Exchange Service (DAAD) for a scholarship in the PROMOS programme.

Code Availability. The implementation of the adopted phase-field fatigue model, the cyclic solver as well as the proposed cycle-jump scheme are available in the open-source library GRIPHFITH [12] and can be accessed at <https://gitlab.ethz.ch/compmech/GRIPHFITH>.

Appendix A Correction and validation of the smeared crack length approach

In the following, we investigate and correct the influence of a non-optimal phase-field profile on the smeared crack length approach; then, we use a representative numerical test to validate it.

A.1 Correction of the smeared crack length

As explained in Section 4.2, the assumption of an optimal phase-field profile may not necessarily hold in the numerical context, leading to a wrong estimation of the crack length. This is due to the following reasons:

- the irreversibility condition of the phase field $\dot{d} \geq 0$;
- the phase field around the crack tip does not correspond to the revolved optimal half-profile, as also mentioned by Freddi in [18]. The effect of the crack tip on the phase-field regularization is systematically studied in [51], and its influence is shown to be especially large for smaller cracks;
- the discretization error;
- the phase-field fatigue model, by locally degrading the fracture toughness of the material, leads to a heterogeneous \mathcal{G}_c , whose effect on the phase-field profile is studied in [66].

In the following, we introduce corrections for the first three systematic and predictable errors.

A.1.1 Error due to damage irreversibility

First, we study the influence of the irreversibility condition $\dot{d} \geq 0$. We consider a 1D bar of length $2L \gg 2\ell$, clamped at one end and subjected to a prescribed displacement \bar{u} at the other end, see Fig. A1a. The behavior of the bar is thoroughly discussed by Pham and Marigo in [54, 57, 56]; here we only briefly outline some main results which are useful for the purpose of our correction. First, starting from an undamaged condition and loading the bar under displacement control, we obtain a solution with homogeneous damage,

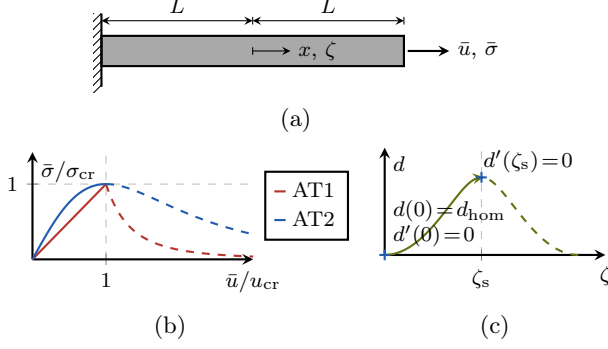


Figure A1: Methodology to obtain the phase-field profiles during localization for a 1D bar (a) with its homogeneous solution (b) and constraints for the semi-analytical solution (c).

reported in terms of normalized stress-displacement response in Fig. A1b. When the peak stress is reached, the phase field attains the value [57]

$$d_{\text{hom}} = \begin{cases} 0 & \text{AT1} \\ 0.25 & \text{AT2} \end{cases} \quad (\text{A1})$$

after which the homogeneous solution becomes unstable (assuming a sufficiently long bar, $L \gg \ell$). At this point, damage localization occurs at an arbitrary location in the bar. During progressive localization, the maximum phase-field value increases monotonically and a snap-back occurs, so that following the behavior requires a switch to (decreasing) stress control with $\bar{\sigma}$. As follows, we compute the intermediate localization profiles during this stage, starting with the homogeneous solution $d = d_{\text{hom}}$ valid at the stress peak, and define their envelope as the ‘irreversible’ phase-field profile. This allows us to then evaluate the discrepancy between this profile and the optimal profile, which can be obtained analytically by ignoring the irreversibility condition (see e.g. [22] for the detailed derivation).

To do so, we adopt a semi-analytical approach similar to those in [53, 66]. We start by writing the damage criterion (6a), here considered as an equality since the phase field is evolving, i.e. $\dot{d} > 0$. Due to the stress control required during the localization stage, the damage criterion is expressed in terms of stress by introducing the compliance $S(d) := 1/E(d)$, with $E(d) = g(d)E_0$, which leads to

$$\frac{1}{2} S'(d) \bar{\sigma}^2 = \frac{G_c}{c_w} \left(\frac{w'(d)}{\ell} - 2\ell d'' \right). \quad (\text{A2})$$

Introducing the non-dimensional coordinate $\zeta := x/\ell$ and the non-dimensional stress $\varrho := \bar{\sigma}/\sigma_{\text{cr}}$, with

$$\sigma_{\text{cr}} = \begin{cases} \sqrt{\frac{3E_0 G_c}{8\ell}} & \text{AT1} \\ \frac{3}{16} \sqrt{\frac{3E_0 G_c}{\ell}} & \text{AT2} \end{cases}, \quad (\text{A3})$$

yields the non-dimensional damage criterion

$$\begin{cases} \frac{1}{(1-d)^3} \varrho^2 = 1 - 2d'' & \text{AT1} \\ \frac{27}{128(1-d)^3} \varrho^2 = 2d - 2d'' & \text{AT2} \end{cases} \quad (\text{A4})$$

which we solve numerically for half of the domain with initial conditions

$$d(\zeta = 0) = d_{\text{hom}} \quad \text{and} \quad d'(\zeta = 0) = 0. \quad (\text{A5})$$

Here we are assuming that outside of the localization zone, the phase field takes the value of the homogeneous solution at peak stress d_{hom} , due to the irreversibility of the damage accumulated during the homogeneous stage. This is in contrast to the reversible case considered in [57], where the phase field is assumed to vanish outside the localization zone. For the AT2 model, the initial condition of a vanishing first derivative is relaxed by setting $d'(0) = 10^{-12}$ to avoid numerical difficulties due to the infinite support. Since we do not know the width of the localization profile, we need one additional condition; denoting the half-width as ζ_s , we impose $d'(\zeta_s) = 0$ (see Fig. A1c).

The irreversible phase-field profiles obtained with this procedure and centered in the middle of the bar are depicted in Fig. A2. As evident for the AT1 model in Fig. A2a, the support of the irreversible profile is slightly wider than that of the optimal profile, and the difference in area is +4.2 %, filled in red in Fig. A2c. Only for values of $d \gtrapprox 0.5$ the two profiles nearly coincide. A similar but much stronger effect can be observed for the AT2 model, see Fig. A2b, where the large homogeneous solution causes major deviations from the optimal phase-field profile. In this case, it is only for values of $d \gtrapprox 0.75$ that the two profiles nearly coincide. Clearly, this behavior depends on the homogeneous solution; while this is known for the 1D bar, it is no longer valid for a general 2D or 3D case. Further, since the localized solutions occur during a snap-back, they cannot be captured by a numerical solution scheme without a stress-controlled or an arc-length controlled solver. However, they are more likely to occur in the fatigue context due to the continuous decrease of the fracture toughness.

Due to the dependency of the areal difference on the homogeneous solution which cannot be determined *a priori* in a general case, instead of introducing a factor

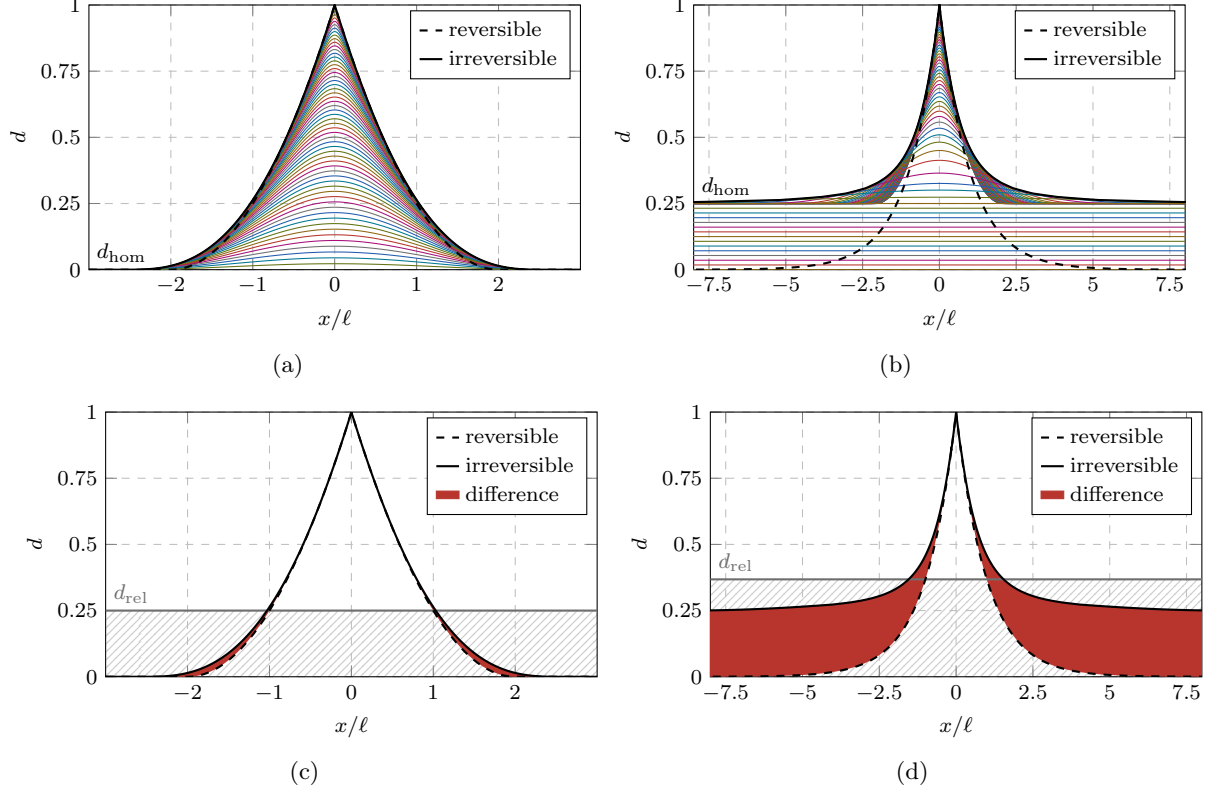


Figure A2: Irreversible phase-field profiles and deviation from optimal profile for the AT1 (a, c) and AT2 (b, d) model, respectively.

to correct the smeared crack length approach, we adopt the approach of ignoring the portion of the phase-field profile below a threshold d_{rel} , such that the effect of irreversibility in the remaining profile is negligible. As depicted in in Figs. A2c and A2d, we choose d_{rel} as the level of damage at $x = \pm \ell$ for the optimal profile

$$d_{\text{rel}} = \begin{cases} 0.25 & \text{AT1} \\ \exp(-1) \approx 0.368 & \text{AT2} \end{cases} \quad (\text{A6})$$

This choice represents a compromise between a small influence of the irreversibility on the compared profiles and the robustness of the approach, since the higher the threshold value, the less points of the numerical solution contribute to the numerical phase-field integral D_{num} . Accordingly, the modified definition of the smeared crack length is

$$a = \begin{cases} \frac{D_{\text{num}}(d) - k\pi\frac{11}{48}\ell^2}{\frac{7}{6}\ell} & \forall d \geq d_{\text{rel}} & \text{AT1} \\ \frac{D_{\text{num}}(d) - k\pi\ell^2(1 - 2\exp(-1))}{2\ell(1 - \exp(-1))} & \forall d \geq d_{\text{rel}} & \text{AT2} \end{cases} \quad (\text{A7})$$

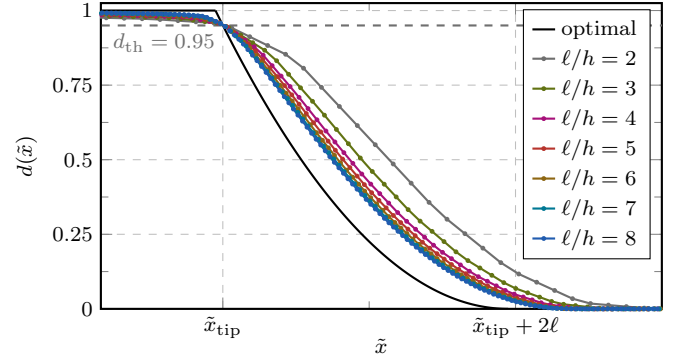


Figure A3: Study of the crack tip and discretization error with the interpolated phase field along the crack path \tilde{x} .

A.1.2 Crack tip and discretization error

Next to the irreversibility, the crack tip and discretization errors cause deviations from the optimal phase-field profile [18, 51], which are illustrated in Fig. A3. Evidently, the profile around the crack tip is not only different from the optimal profile, but it also depends on the FE mesh (discretization error). These errors cannot be corrected exactly due to the inherent numerical approximation, but their systematic influence can be minimized by introducing empirical correction factors. We use one correction factor for the

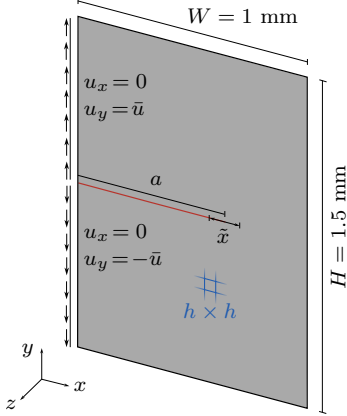


Figure A4: Geometry and boundary conditions for the specimen to determine the correction factors.

crack tip contribution c_{tip} and one for the contribution of the crack length c_{ext} ,

$$a = \frac{D_{\text{num}}(d) - kc_{\text{tip}}D_{\text{tip}}(\ell)}{c_{\text{ext}}D_{\text{ext}}(\ell)}. \quad (\text{A8})$$

To determine these correction factors empirically, we use the specimen in Fig. A4. On the left boundary, the displacement is fixed in the x -direction, while the upper and lower halves of the left edge are pulled apart under displacement control to obtain the nucleation and propagation of a straight crack in the middle of the specimen. We adopt $E = 210$ MPa, $\nu = 0.3$, $\mathcal{G}_c = 0.0027$ MPa mm), no energy decomposition and plane-strain conditions. Furthermore, we use the penalty method [22] with $\text{TOL}_{\text{ir}} = 10^{-6}$ to enforce irreversibility of the phase field, and compute the smeared crack length using the $L1$ -norm approximation (28) due to the uniform discretization of the phase-field support. To provide a comprehensive study of the crack tip and discretization error, all combinations of $\ell = 0.01, 0.02, 0.03, 0.04, 0.05, 0.06$ mm and the element sizes $\ell/h = 2, 3, 4, 5, 6, 7, 8$ are investigated. Although the outer dimensions are chosen large enough with respect to ℓ , we only consider the phase-field solution in the subdomain with $x > W/5$ and up to a crack length of $a = W/2$ to avoid boundary effects. We use the interpolated crack tip method outlined in Fig. 14 to calibrate the smeared crack length approach. In particular, the correction factor for the crack tip contribution c_{tip} is computed by comparing the point at which the first full crack development is obtained, while the correction factor for the crack extent c_{ext} is determined such that the crack growth rates coincide in a best-fit sense.

The obtained correction factors are visualized in dependency of the regularization parameter ℓ and the discretization parameter ℓ/h in Fig. A5. We can

Table A1: Correction factors for the crack tip and discretization error, obtained with bilinear quadrilateral elements, $d_{\text{th}} = 0.95$ and considering irreversibility by means of (A6).

regularization	ℓ/h	c_{tip}	c_{ext}
AT1	2	3.171	1.582
	3	2.244	1.390
	4	1.846	1.302
	5	1.680	1.249
	6	1.539	1.211
	7	1.468	1.187
	8	1.416	1.171
AT2	2	3.931	1.604
	3	2.875	1.411
	4	2.410	1.323
	5	2.136	1.271
	6	2.014	1.228
	7	1.893	1.204
	8	1.812	1.185

observe that the correction factors are virtually independent of ℓ , while all of them show the same trend in the direction of ℓ/h , converging towards one value with increasing ℓ/h . For the various ℓ/h , we take the correction factors c_{tip} and c_{ext} as average of the values for different length scale parameters ℓ , as indicated with the black lines in Fig. A5. They are listed in Tab. A1, meaning that the correction of the smeared crack length must be set according to the chosen discretization for a most accurate measurement of the smeared crack length approach. These values were obtained already accounting for the irreversibility, using bilinear quadrilateral elements. We remark that the correction factors might depend on the particular FE implementation and chosen tolerances. Also, other element types and orders may require a different correction factor.

A.2 Validation of the smeared crack length approach

Finally, we validate the concept of the smeared crack length by comparing it to the discrete and interpolated crack tip tracking algorithms outlined in Fig. 14. In particular, we use the CT test setup of Section 5.2 and depicted in Fig. 15 for a fatigue computation at the load level $P_{\text{max}} = 110$ N. Further, we compare the smeared crack length computed by numerically integrating the phase-field solution to its approximation using the $L1$ -norm of the phase-field solution. As before, the interpolated crack tip method (Fig. 14) is considered to be the most accurate in cases where the crack path is straight and known *a priori*, such as for the test at hand.

Comparing the measured crack lengths of the three different approaches in Figs. A6a and A6b, we can observe that the discrete and interpolated crack lengths virtually coincide. The smeared crack length in its uncorrected form shows a significant deviation especially

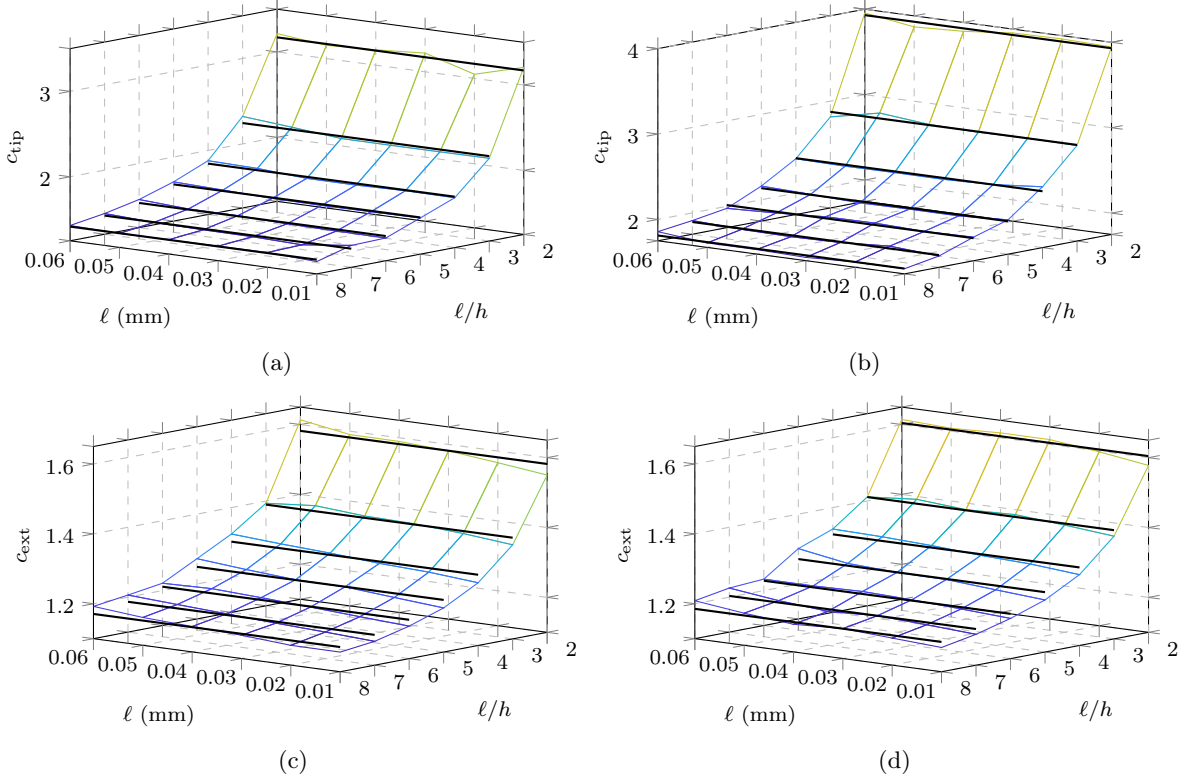


Figure A5: Correction factors of tip and length contributions for the smeared crack length approach as a function of the length scale ℓ and the ℓ/h ratio with the AT1 (a, c) and AT2 model (b, d), respectively. The data points are connected with lines for better visibility.

towards the end of the fatigue life, which can be attributed to the deviation due to the irreversibility as well as the regularization and crack tip error accumulating over time. For the AT2 model additionally, a significant deviation can be observed already from the beginning, which is due to the homogeneous solution acting as an artificial initial crack length. Accounting for all these factors, the smeared crack length measurements in their corrected form show a good agreement with the other two crack tip tracking algorithms. The remaining deviations of the corrected smeared crack length are attributed to the facts that the correction factors were obtained with homogeneous distribution of the fracture toughness and with the penalty method [22], whereas here the fatigue effects lead to a heterogeneous $f(\bar{\alpha})\mathcal{G}_c$ and the history-variable approach [44] is used for irreversibility. The approximation of the smeared crack length approach with the $L1$ -norm shows a good agreement with the smeared crack length obtained with numerical integration proving its validity, which is due to the almost perfectly uniform discretization of the phase-field support in this specific test.

Comparing the measured crack growth rates \dot{a} in Figs. A6c and A6d, the differences of the compared approaches become apparent: the discrete crack length

monitors exclusively a crack growth rate corresponding to the element size (here mostly $da = 0.04$ mm), while in most cycles, it records $da = 0$ mm. In contrast, the interpolated crack tip tracking approach yields a more precise measurement of the crack growth rate since the crack is straight and known *a priori*, although the measurement is subject to oscillations from cycle to cycle. The smeared crack approach matches the interpolated crack growth rate very well, while the uncorrected smeared crack length overestimates the crack growth rate especially towards the end of the fatigue life. The smeared crack length gives overall the most stable trend, hence making it suitable for the novel acceleration scheme which relies on a robust crack length measurement in stage III, while its approximation with the $L1$ -norm is subject to slightly more instabilities. This is why we use the smeared crack length as computed with numerical integration for the proposed cycle-jump scheme, since the LLSQ fit and thus the algorithm performs better if the underlying crack growth rate evaluation is more robust.

To finally showcase the capability of the smeared crack length concept, the crack growth rate curves are shown in Figs. A6e and A6f for the different crack tip tracking methods. While the predictions from the discrete and interpolated crack tip show good agreement,

with the former showing slightly more oscillations, the smeared crack length approach matches both conventional approaches with only slight deviations towards the final stage of unstable crack propagation. Again, the uncorrected smeared crack length shows significant deviations especially for the AT2 dissipation function, highlighting the importance of the correction factors. Overall, these results emphasize that the smeared crack length concept in its corrected form can substitute a conventional crack tip tracking algorithm.

References

- [1] Alessi R, Ulloa J (2023) Endowing griffith's fracture theory with the ability to describe fatigue cracks. *Engineering Fracture Mechanics* 281. <https://doi.org/10.1016/j.engfracmech.2023.109048>
- [2] Alessi R, Vidoli S, De Lorenzis L (2018) A phenomenological approach to fatigue with a variational phase-field model: The one-dimensional case. *Engineering Fracture Mechanics* 190:53–73. <https://doi.org/10.1016/j.engfracmech.2017.11.036>
- [3] Ambati M, Heinzmann J, Seiler M, et al (2022) Phase-field modeling of brittle fracture along the thickness direction of plates and shells. *International Journal for Numerical Methods in Engineering* 123(17):4094–4118. <https://doi.org/10.1002/nme.7001>
- [4] Amendola G, Fabrizio M, Golden JM (2016) Thermomechanics of damage and fatigue by a phase field model. *Journal of Thermal Stresses* 39(5):487–499. <https://doi.org/10.1080/01495739.2016.1152140>
- [5] Amor H, Marigo JJ, Maurini C (2009) Regularized formulation of the variational brittle fracture with unilateral contact: Numerical experiments. *Journal of the Mechanics and Physics of Solids* 57(8):1209–1229. <https://doi.org/10.1016/j.jmps.2009.04.011>
- [6] Aygün S, Wiegold T, Klinge S (2021) Coupling of the phase field approach to the armstrong-frederick model for the simulation of ductile damage under cyclic load. *International Journal of Plasticity* 143. <https://doi.org/10.1016/j.ijplas.2021.103021>
- [7] Bhattacharyya M, Fau A, Nackenhorst U, et al (2018) A multi-temporal scale model reduction approach for the computation of fatigue damage. *Computer Methods in Applied Mechanics and Engineering* 340:630–656. <https://doi.org/10.1016/j.cma.2018.06.004>
- [8] Boldrini J, Barros de Moraes E, Chiarelli L, et al (2016) A non-isothermal thermodynamically consistent phase field framework for structural damage and fatigue. *Computer Methods in Applied Mechanics and Engineering* 312:395–427. <https://doi.org/10.1016/j.cma.2016.08.030>
- [9] Bourdin B, Francfort G, Marigo JJ (2000) Numerical experiments in revisited brittle fracture. *Journal of the Mechanics and Physics of Solids* 48(4):797–826. [https://doi.org/10.1016/S0022-5096\(99\)00028-9](https://doi.org/10.1016/S0022-5096(99)00028-9)
- [10] Caputo M, Fabrizio M (2015) Damage and fatigue described by a fractional derivative model. *Journal of Computational Physics* 293:400–408. <https://doi.org/10.1016/j.jcp.2014.11.012>
- [11] Carrara P, Ambati M, Alessi R, et al (2020) A framework to model the fatigue behavior of brittle materials based on a variational phase-field approach. *Computer Methods in Applied Mechanics and Engineering* 361(112731). <https://doi.org/10.1016/j.cma.2019.112731>
- [12] Carrara P, Rybinski M, Bräunlich G, et al (2023) GRIPFH. ETH Zürich, URL <https://gitlab.ethz.ch/compmech/GRIPFH>
- [13] Chen Y, Vasiukov D, Gélébart L, et al (2019) A fft solver for variational phase-field modeling of brittle fracture. *Computer Methods in Applied Mechanics and Engineering* 349:167–190. <https://doi.org/10.1016/j.cma.2019.02.017>
- [14] Cheng J, Hu X, Kirka M (2022) A cycle-jump acceleration method for the crystal plasticity simulation of high cycle fatigue of the metallic microstructure. *International Journal of Fatigue* 165:107185. <https://doi.org/10.1016/j.ijfatigue.2022.107185>
- [15] Cojocaru D, Karlsson A (2006) A simple numerical method of cycle jumps for cyclically loaded structures. *International Journal of Fatigue* 28(12):1677–1689. <https://doi.org/10.1016/j.ijfatigue.2006.01.010>
- [16] De Lorenzis L, Maurini C (2022) Nucleation under multi-axial loading in variational phase-field models of brittle fracture. *International Journal*

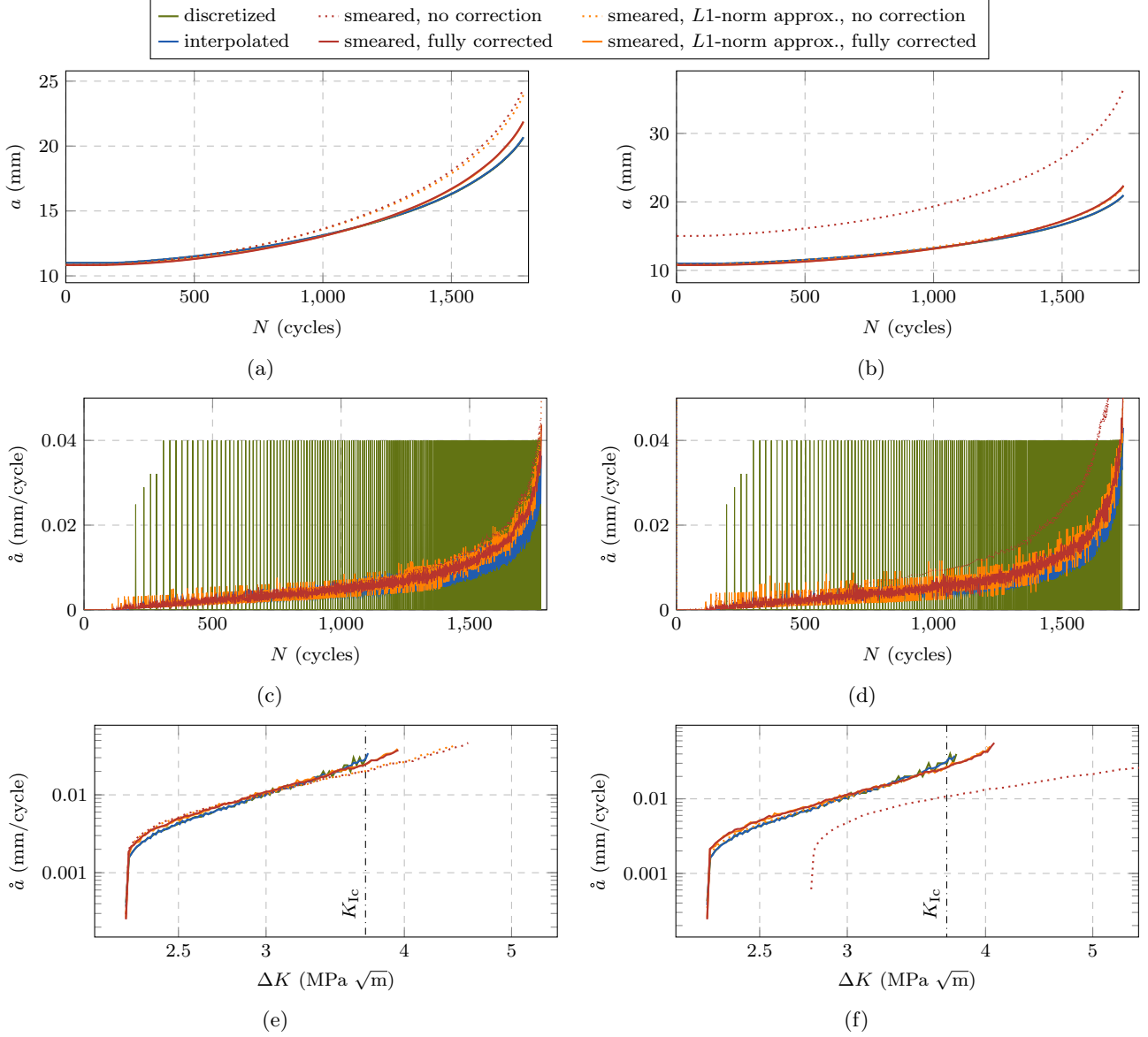


Figure A6: Validation of the smeared crack approach with a CT test in terms of crack length (a, b), crack growth (c, d) and crack growth rate curve (e, f), as obtained with the different crack tip tracking algorithms for the AT1 (a,c,e) and the AT2 model (b,d,f), respectively.

of Fracture 237:61–81. <https://doi.org/10.1007/s10704-021-00555-6>

- [17] Francfort G, Marigo JJ (1998) Revisiting brittle fracture as an energy minimization problem. *Journal of the Mechanics and Physics of Solids* 46(8):1319–1342. [https://doi.org/10.1016/S0022-5096\(98\)00034-9](https://doi.org/10.1016/S0022-5096(98)00034-9)
- [18] Freddi F (2019) Fracture energy in phase field models. *Mechanics Research Communications* 96:29–36. <https://doi.org/10.1016/j.mechrescom.2019.01.009>

- [19] Freddi F, Mingazzi L (2023) Adaptive mesh refinement for the phase field method: A fenics implementation. *Applications in Engineering Science* 14. <https://doi.org/10.1016/j.apples.2023.100127>
- [20] Freddi F, Royer-Carfagni G (2010) Regularized variational theories of fracture: A unified approach. *Journal of the Mechanics and Physics of Solids* 58(8):1154–1174. <https://doi.org/10.1016/j.jmps.2010.02.010>
- [21] Gerasimov T, De Lorenzis L (2016) A line search assisted monolithic approach for phase-field computing of brittle fracture. *Computer Methods in*

- Applied Mechanics and Engineering 312:276–303. <https://doi.org/10.1016/j.cma.2015.12.017>
- [22] Gerasimov T, De Lorenzis L (2019) On penalization in variational phase-field models of brittle fracture. *Computer Methods in Applied Mechanics and Engineering* 354:990–1026. <https://doi.org/10.1016/j.cma.2019.05.038>
- [23] Griffith AA (1921) The phenomena of rupture and flow in solids. *Philosophical Transactions of the Royal Society of London* 221:163–198. URL <https://www.jstor.org/stable/91192>
- [24] Grossman-Ponemon BE, Mesgarnejad A, Karma A (2022) Phase-field modeling of continuous fatigue via toughness degradation. *Engineering Fracture Mechanics* 264(108255). <https://doi.org/10.1016/j.engfracmech.2022.108255>
- [25] Gupta A, Krishnan UM, Mandal TK, et al (2022) An adaptive mesh refinement algorithm for phase-field fracture models: Application to brittle, cohesive, and dynamic fracture. *Computer Methods in Applied Mechanics and Engineering* 399. <https://doi.org/10.1016/j.cma.2022.115347>
- [26] Hansen-Dörr AC, Dammaß F, de Borst R, et al (2020) Phase-field modeling of crack branching and deflection in heterogeneous media. *Engineering Fracture Mechanics* 232:107004. <https://doi.org/10.1016/j.engfracmech.2020.107004>
- [27] Hasan MM, Baxevis T (2021) A phase-field model for low-cycle fatigue of brittle materials. *International Journal of Fatigue* 150(106297). <https://doi.org/10.1016/j.ijfatigue.2021.106297>
- [28] Haverorth G, Vale M, Bittencourt M, et al (2020) A non-isothermal thermodynamically consistent phase field model for damage, fracture and fatigue evolutions in elasto-plastic materials. *Computer Methods in Applied Mechanics and Engineering* 364(112962). <https://doi.org/10.1016/j.cma.2020.112962>
- [29] Hennig P, Ambati M, De Lorenzis L, et al (2018) Projection and transfer operators in adaptive isogeometric analysis with hierarchical B-splines. *Computer Methods in Applied Mechanics and Engineering* 334:313–336. <https://doi.org/10.1016/j.cma.2018.01.017>
- [30] Hosseini ZS, Dadfarnia M, Somerday BP, et al (2018) On the theoretical modeling of fatigue crack growth. *Journal of the Mechanics and Physics of Solids* 121:341–362. <https://doi.org/10.1016/j.jmps.2018.07.026>
- [31] Jacon A, Prabel B, Molnár G, et al (2023) Adaptive mesh refinement and cycle jumps for phase-field fatigue fracture modeling. *Finite Elements in Analysis and Design* 224:104004. <https://doi.org/10.1016/j.finel.2023.104004>
- [32] Kalina M, Schneider T, Brummund J, et al (2023) Overview of phase-field models for fatigue fracture in a unified framework. *Engineering Fracture Mechanics* 288:109318. <https://doi.org/10.1016/j.engfracmech.2023.109318>
- [33] Khalil Z, Elghazouli AY, Martínez-Pañeda E (2022) A generalised phase field model for fatigue crack growth in elastic-plastic solids with an efficient monolithic solver. *Computer Methods in Applied Mechanics and Engineering* 388(114286). <https://doi.org/10.1016/j.cma.2021.114286>
- [34] Kiewel H, Aktaa J, Munz D (2000) Application of an extrapolation method in thermocyclic failure analysis. *Computer Methods in Applied Mechanics and Engineering* 182(1-2):55–71. [https://doi.org/10.1016/S0045-7825\(99\)00085-7](https://doi.org/10.1016/S0045-7825(99)00085-7)
- [35] Kristensen PK, Martínez-Pañeda E (2020) Phase field fracture modelling using quasi-newton methods and a new adaptive step scheme. *Theoretical and Applied Fracture Mechanics* 107. <https://doi.org/10.1016/j.tafmec.2019.102446>
- [36] Kristensen PK, Golahmar A, Martínez-Pañeda E, et al (2023) Accelerated high-cycle phase field fatigue predictions. *European Journal of Mechanics - A/Solids* 100. <https://doi.org/10.1016/j.euromechsol.2023.104991>
- [37] Lancioni G, Royer-Carfagni G (2009) The variational approach to fracture mechanics. a practical application to the french panthéon in paris. *Journal of Elasticity* 95:1–30. <https://doi.org/10.1007/s10659-009-9189-1>
- [38] Lemaitre J, Daghri I (1994) Damage 90: A post processor for crack initiation. *Computer Methods in Applied Mechanics and Engineering* 115:197–232. [https://doi.org/10.1016/0045-7825\(94\)90060-4](https://doi.org/10.1016/0045-7825(94)90060-4)
- [39] Lemaitre J, Sermage J, Desmorat R (1999) A two scale damage concept applied to fatigue. *International Journal of Fracture* 97:67–81. <https://doi.org/10.1023/A:1018641414428>

- [40] Li Z, Shen Y, Han F, et al (2021) A phase field method for plane-stress fracture problems with tension-compression asymmetry. *Engineering Fracture Mechanics* 257. <https://doi.org/10.1016/j.engfracmech.2021.107995>
- [41] Lo YS, Borden MJ, Ravi-Chandar K, et al (2019) A phase-field model for fatigue crack growth. *Journal of the Mechanics and Physics of Solids* 132(103684). <https://doi.org/10.1016/j.jmps.2019.103684>
- [42] Loew PJ, Poh LH, Peters B, et al (2020) Accelerating fatigue simulations of a phase-field damage model for rubber. *Computer Methods in Applied Mechanics and Engineering* 370(113247). <https://doi.org/10.1016/j.cma.2020.113247>
- [43] Marigo JJ (2023) Modelling of fracture by cohesive force models: A path to pursue. *European Journal of Mechanics - A/Solids* 102. <https://doi.org/10.1016/j.euromechsol.2023.105088>
- [44] Miehe C, Hofacker M, Welschinger F (2010) A phase field model for rate-independent crack propagation: Robust algorithmic implementation based on operator splits. *Computer Methods in Applied Mechanics and Engineering* 199:2765–2778. <https://doi.org/10.1016/j.cma.2010.04.011>
- [45] Miehe C, Welschinger F, Hofacker M (2010) Thermodynamically consistent phase-field models of fracture: Variational principles and multi-field fe implementations. *International Journal for Numerical Methods in Engineering* 83(10):1273–1311. <https://doi.org/10.1002/nme.2861>
- [46] Moslemian R, Karlsson A, Berggreen C (2011) Accelerated fatigue crack growth simulation in a bimaterial interface. *International Journal of Fatigue* 33(12):1526–1532. <https://doi.org/10.1016/j.ijfatigue.2011.06.006>
- [47] Nesnas K, Saanouni K (2000) A cycle jumping scheme for numerical integration of coupled damage and viscoplastic models for cyclic loading paths. *Revue Européenne des Éléments Finis* 9(8):865–891. <https://doi.org/10.1080/12506559.2000.10511493>
- [48] Nguyen T, Yvonnet J, Zhu QZ, et al (2015) A phase field method to simulate crack nucleation and propagation in strongly heterogeneous materials from direct imaging of their microstructure. *Engineering Fracture Mechanics* 139:18–39. <https://doi.org/10.1016/j.engfracmech.2015.03.045>
- [49] Olesch D, Kuhn C, Schlüter A, et al (2021) Adaptive numerical integration of exponential finite elements for a phase field fracture model. *Computational Mechanics* 67(3):811–821. <https://doi.org/10.1007/s00466-020-01964-5>
- [50] Oskay C, Fish J (2004) Fatigue life prediction using 2-scale temporal asymptotic homogenization. *International Journal for Numerical Methods in Engineering* 61(3):329–359. <https://doi.org/10.1002/nme.1069>
- [51] Pascale P, Vemaganti K (2023) The systematic nature of regularization error in phase field modeling: Implications for crack nucleation and propagation. *International Journal of Fracture* 239(2):189–209. <https://doi.org/10.1007/s10704-022-00670-y>
- [52] Peerlings RHJ, Brekelmans WAM, de Borst R, et al (2000) Gradient-enhanced damage modelling of high-cycle fatigue. *International Journal for Numerical Methods in Engineering* 49(12):1547–1569. [https://doi.org/10.1002/1097-0207\(20001230\)49:12<1547::AID-NME16>3.0.CO;2-D](https://doi.org/10.1002/1097-0207(20001230)49:12<1547::AID-NME16>3.0.CO;2-D)
- [53] Pham K, Marigo JJ (2009) Construction and analysis of localized responses for gradient damage models in a 1d setting. *Vietnam Journal of Mechanics* 31(3-4). <https://doi.org/10.15625/0866-7136/31/3-4/5651>
- [54] Pham K, Marigo JJ (2010) Approche variationnelle de l'endommagement : I. les concepts fondamentaux. *Comptes Rendus Mécanique* 338(4):191–198. <https://doi.org/10.1016/j.crme.2010.03.009>
- [55] Pham K, Marigo JJ (2010) Approche variationnelle de l'endommagement : II. les modèles à gradient. *Comptes Rendus Mécanique* 338(4):199–206. <https://doi.org/10.1016/j.crme.2010.03.012>
- [56] Pham K, Marigo JJ (2013) From the onset of damage to rupture: Construction of responses with damage localization for a general class of gradient damage models. *Continuum Mechanics and Thermodynamics* 25(2-4):147–171. <https://doi.org/10.1007/s00161-011-0228-3>
- [57] Pham K, Amor H, Marigo JJ, et al (2011) Gradient damage models and their use to approximate

- brittle fracture. *International Journal of Damage Mechanics* 20(4):618–652. <https://doi.org/10.1177/1056789510386852>
- [58] Pham K, Marigo JJ, Maurini C (2011) The issues of the uniqueness and the stability of the homogeneous response in uniaxial tests with gradient damage models. *Journal of the Mechanics and Physics of Solids* 59(6):1163–1190. <https://doi.org/10.1016/j.jmps.2011.03.010>
- [59] Schreiber C, Kuhn C, Müller R, et al (2020) A phase field modeling approach of cyclic fatigue crack growth. *International Journal of Fracture* 225(1):89–100. <https://doi.org/10.1007/s10704-020-00468-w>
- [60] Seiler M, Linse T, Hantschke P, et al (2020) An efficient phase-field model for fatigue fracture in ductile materials. *Engineering Fracture Mechanics* 224(106807). <https://doi.org/10.1016/j.engfracmech.2019.106807>
- [61] Seleš K, Aldakheel F, Tonković Z, et al (2021) A general phase-field model for fatigue failure in brittle and ductile solids. *Computational Mechanics* 67(5):1431–1452. <https://doi.org/10.1007/s00466-021-01996-5>
- [62] Seleš K, Tomić Z, Tonković Z (2021) Micro-crack propagation under monotonic and cyclic loading conditions using generalised phase-field formulation. *Engineering Fracture Mechanics* 255(107973). <https://doi.org/10.1016/j.engfracmech.2021.107973>
- [63] Tan Y, He Y, Li X, et al (2022) A phase field model for fatigue fracture in piezoelectric solids: A residual controlled staggered scheme. *Computer Methods in Applied Mechanics and Engineering* 399(115459). <https://doi.org/10.1016/j.cma.2022.115459>
- [64] Ulloa J, Wambacq J, Alessi R, et al (2021) Phase-field modeling of fatigue coupled to cyclic plasticity in an energetic formulation. *Computer Methods in Applied Mechanics and Engineering* 373. <https://doi.org/10.1016/j.cma.2020.113473>
- [65] Van Paepegem W, Degrieck J, De Baets P (2001) Finite element approach for modelling fatigue damage in fibre-reinforced composite materials. *Composites Part B: Engineering* 32(7):575–588. [https://doi.org/10.1016/S1359-8368\(01\)00038-5](https://doi.org/10.1016/S1359-8368(01)00038-5)
- [66] Vicentini F, Carrara P, De Lorenzis L (2023) Phase-field modeling of brittle fracture in heterogeneous bars. *European Journal of Mechanics - A/Solids* 97. <https://doi.org/10.1016/j.euromechsol.2022.104826>
- [67] Vicentini F, Zolesi C, Carrara P, et al (2024) On the energy decomposition in variational phase-field models for brittle fracture under multi-axial stress states. *International Journal of Fracture* <https://doi.org/10.1007/s10704-024-00763-w>
- [68] Yan S, Schreiber C, Müller R (2022) An efficient implementation of a phase field model for fatigue crack growth. *International Journal of Fracture* pp 47–60. <https://doi.org/10.1007/s10704-022-00628-0>
- [69] Zeng J, Zhang M, Yang E, et al (2022) A tracking strategy for multi-branched crack tips in phase-field modeling of dynamic fractures. *International Journal for Numerical Methods in Engineering* 123(3):844–865. <https://doi.org/10.1002/nme.6879>